UNIVERSIDADE
BEIRA INTERIOR

3D Simulation of a Detonation Wave in a Rotating Detonation Engine

(Versão final após defesa)

Francisca Antunes Serras

Dissertação para obtenção do Grau de Mestre em
Engenharia Aeronáutica
(Mestrado Integrado)

Orientador: Prof. Doutor Francisco Miguel Ribeiro Proença Brójo

janeiro de 2025

Declaração de Integridade

Eu, Francisca Antunes Serras, que abaixo assino, estudante com o número de inscrição 43386 do Mestrado Integrado em Engenharia Aeronáutica da Faculdade de Engenharia, declaro ter desenvolvido o presente trabalho e elaborado o presente texto em total consonância com o **Código de Integridades da Universidade da Beira Interior.**

Mais concretamente afirmo não ter incorrido em qualquer das variedades de Fraude Académica, e que aqui declaro conhecer, que em particular atendi à exigida referenciação de frases, extratos, imagens e outras formas de trabalho intelectual, e assumindo assim na íntegra as responsabilidades da autoria.

Universidade da Beira Interior, Covilhã 07/01/2025

Assinado por: **Francisca Antunes Serras**
Num. de Identificação: 14473635
Data: 2025.01.07 20:15:22+00'00'

Dedicated to my Family

Acknowledgments

I extend my heartfelt gratitude to Professor Francisco Brójo and to João Pedro Cristóvão Silva for their unwavering support throughout the entirety of my dissertation journey and for introducing me to this compelling subject. Undertaking the simulation of a detonation wave in a rotating detonation engine presented significant challenges, yet it equipped me with invaluable mathematical and problem-solving skills that are unique to this endeavour. I am sincerely thankful for the guidance and assistance provided.

I also want to express my deep appreciation to my mother, father, and sister for their inexhaustible academic and financial support during my degree at the University of Beira Interior. Their presence and assistance at every step of my journey were truly invaluable.

Furthermore, I am grateful to all my friends who accompanied me through this Master's Degree journey. Whether it was the late-night study sessions or the moments of joy we shared in the enchanting city of Covilhã, the bond we formed and the memories we created will forever hold a special place in my heart. A special acknowledgment goes to my boyfriend, Miguel Moreira, whose constant encouragement and unwavering support urged me to persevere, even during the most challenging phases of my dissertation, and always helped throughout the entire degree. To each and every one of you, I extend my heartfelt gratitude.

Resumo

O desenvolvimento de sistemas de propulsão eficientes é um aspeto crítico na engenharia aeroespacial, e os motores de detonação rotativa (RDEs) apresentam um avanço promissor em relação às tecnologias de propulsão convencionais devido às suas configurações compactas e alta eficiência térmica. Nesta dissertação, são apresentados e discutidos os resultados de uma simulação tridimensional de um motor de detonação rotativa utilizando como combustível uma mistura de hidrogénio e ar. Resultados de uma simulação utilizando uma mistura de hidrogénio e oxigénio são também apresentados. As simulações foram feitas utilizando o ANSYS Fluent e todos os outros detalhes da metodologia utilizada são explicados neste trabalho.

Os principais aspetos da simulação incluem a formulação da turbulência e da detonação, as condições de operação do motor, e o posterior impacto destas condições operacionais no próprio desempenho do motor, nomeadamente, na iniciação e estabilização da onda de detonação. A análise computacional revela aspetos críticos sobre os campos de pressão, temperatura, velocidade de chama, tração e impulso específico. Obteve-se uma operação de motor estável com quatro voltas da onda de detonação à câmara de combustão. Verificou-se que aquando da utilização de uma mistura de hidrogénio e oxigénio, a detonação não prevaleceu e deflagração ocorreu dentro da câmara. Aquando da utilização de uma mistura de hidrogénio e ar, a detonação ocorreu e o motor entrou em operação estável. A simulação correu por 10220 time steps perfazendo um tempo de simulação de fluido de 1022 microsegundos.

Este trabalho contribui para a otimização de projetos de motores com melhor desempenho e para futuras pesquisas sobre este tema. Os resultados obtidos têm implicações potenciais para o desenvolvimento futuro de sistemas de propulsão de alta eficiência e baixas emissões, abrindo caminho para avanços, principalmente, no setor aeroespacial.

Palavras-Chave

Motor de Detonação Rotativa, Combustão, Detonação, Ondas de Choque, Simulação, CFD, ANSYS Fluent

Abstract

The development of efficient propulsion systems is a critical focus in aerospace engineering, and rotating detonation engines (RDEs) present a promising advancement over conventional propulsion technologies because of their compact configurations and high thermal cycle efficiency. In this dissertation, the results of a three-dimensional simulation of a rotation detonation engine using a mixture of hydrogen and air as fuel are presented and discussed. Results from a simulation using a mixture of hydrogen and oxygen are also presented. The simulations were carried out using ANSYS Fluent and all other details of the methodology used are explained in this work.

Key aspects of the simulation include the formulation of turbulence and detonation, the engine operating conditions, and the subsequent impact of these operating conditions on the engine performance itself, namely, the initiation and stabilization of the detonation wave. The computational analysis reveals critical insights into the pressure and temperature fields, flame speed, thrust and specific impulse. Stable engine operation was achieved and the detonation wave made four revolutions around the combustion chamber. It was found that when using a mixture of hydrogen and oxygen, detonation did not prevail and deflagration occurred inside the annular combustion chamber. When using a mixture of hydrogen and air, detonation occurred and the engine went into stable operation. The simulation ran for 10220 time steps giving a fluid simulation time of 1022 microseconds.

This research contributes to optimizing engine designs with enhanced performance and future research on this matter. The findings have potential implications for the future development of high-efficiency, low-emission propulsion systems, paving the way for advancements, mostly, in the aerospace sector.

Keywords

Rotating Detonation Engine (RDE), Combustion, Detonation, Shock Waves, Simulation, CFD, ANSYS Fluent

Contents

List of Figures

List of Tables

List of Acronyms

3D	Three-Dimensional
AFRL	Air Force Research Laboratory
AUSM	Advection Upstream Splitting Method
CAD	Computer-Aided Design
CFD	Computational Fluid Dynamics
CPU	Central Processing Unit
DARPA	Defense Advanced Research Projects Agency
DBCS	Density-Based Coupled Solver
DNS	Direct Numerical Simulation
DWs	Detonation Waves
ILU	Incomplete LU Factorization
LES	Large Eddy Simulation
MUSCL	Monotone Upstream-Centered Schemes for Conservation Laws
NASA	National Aeronautics and Space Administration
NITA	Non-Iterative Time Advancement
PBCS	Pressure-Based Coupled Solver
PDE	Pulse Detonation Engine
PDF	Probability Density Function
QUICK	Quadratic Upwind Interpolation
RAM	Random Access Memory
RANS	Reynolds-Averaged Navier-Stokes
RDEs	Rotating Detonation Engines
RDTE	Rotating Detonation Turbine Engine
RNG	Renormalization Group
Roe-FDS	Roe Flux-Difference Splitting
SDE	Standing Detonation Engine
SST	Shear Stress Transport
UDF	User-Defined Function
WUT	Warsaw University of Technology
ZND	Zel'dovich - Von Neumann - Döring

List of Symbols

Symbol	Description	Units
A	Area	m^2
c_p	Specific Heat Capacity at Constant Pressure	$J/(kg\ K)$
F	Thrust	N
f	Frequency	Hz
g	Gravitational Acceleration	m/s^2
I_{sp}	Specific Impulse	s
k	Turbulent Kinetic Energy	m^2/s^2
L	Characteristic Linear Dimension	m
M	Mach Number	$-$
$\dot{m}$	Mass Flow Rate	kg/s
p	Pressure	Pa
$\dot{q}$	Heat Flux	W/m^2
R	Universal Gas Constant	$J/(kg\ K)$
Re	Reynolds Number	$-$
s	Entropy	J/K
T	Temperature	K
t	Time	s
V	Velocity	m/s
γ	Adiabatic Index	$-$
δ_{ij}	Kronecker Delta	$-$
ε	Turbulent Dissipation Rate	m^2/s^3
η	Efficiency	$\%$
κ	Thermal Conductivity	$W(mK)^{-1}$
μ	Dynamic Viscosity	$kg(ms)^{-1}$
μ_t	Turbulent Viscosity	$kg(ms)^{-1}$
ν	Prandtl Meyer Angle	$^\circ$
ρ	Density	kg/m^3
τ_{ij}	Shear Stress	Pa
ω	Turbulent-specific Dissipation Rate	s^{-1}

Chapter 1

Introduction

1.1 Motivation

Nowadays, continuing research on new propulsion techniques and engines is vital for the advancement of the aerospace and aeronautical sectors, offering the potential for improved efficiency, reduced environmental impact, and technological innovation.

Rotating Detonation Engines (RDEs) are fundamentally a more compact and efficient method of generating thrust for a diversity of different applications, for example, a variety of military systems including air-to-ground, air-to-air, and surface weapons. These engines are mechanically simpler and have no moving parts which makes them less complex than other commonly used gas turbine engines. Therefore, RDEs are easier to manufacture at a potentially lower cost [1].

RDEs have the potential to improve the efficiency of propulsion systems. The thermodynamic cycles of the detonation combustion could deliver a performance increase of 20% beyond the conventional deflagration combustor (gas turbines and ramjets). The detonative combustor is a prospective technology for high-efficiency power systems in the future, leading to higher thermal efficiency and better fuel consumption [2].

Investigating alternative propulsion technologies contributes to the development of environmentally friendly solutions. The carbon emissions caused by the aviation industry are an urgent problem, greenhouse gas emissions, control of pollutants and efficient energy utilization are future development trends. The performance of a rotating detonation turbine engine (RDTE) can be combined with energy-saving characteristics, under specific combustion chamber pressure ratios, which results in an improvement of up to four times or greater. Also, the fuel consumption rate may decrease by 20% or greater, so the RDTE demonstrates significant application potential, can reduce energy consumption, and improve engine performance [3].

In terms of operational flexibility, the continuous research on RDEs may lead to engines with improved operational flexibility, including better adaptability to varying flight conditions, faster response times, and the ability to operate in a wider range of altitudes and speeds. Additionally, the study of new propulsion systems involves exploring innovative concepts and technologies in areas such as materials science, combustion dynamics, and control systems. The knowledge gained can have broader applications beyond propulsion systems, benefiting

various engineering disciplines.

The desire to contribute, no matter how small, to the progression of civilization, in specific to the industries I love (aeronautical and aerospace industries), serves as a very powerful motivation for writing this dissertation. I hope to contribute to the understanding and development of more efficient and effective RDEs.

1.2 Objectives

The way RDEs work and behave is still being studied by researchers and other students around the world. Therefore, the main goal of this dissertation is to understand and explain the combustion and rotating detonation process and present an operating 3D simulation of a RDE using a mixture of hydrogen and air to understand better how this engine operates and to obtain plots and values that can be useful for other researchers around the world.

To elucidate the dissertation's scope and significance, the pursuit of the primary objective is delineated through a series of steps that actively contribute to the overall learning process. These steps include:

1. Understanding the theoretical concepts of shock waves and combustion;
2. Comprehending combustion with rotating detonation and its differences when comparing against combustion without rotating detonation;
3. Acquiring fundamental concepts of Computational Fluid Dynamics (CFD) and turbulence;
4. Explaining RDEs sizing method and the influence of different parameters;
5. Defining boundary conditions, requirements, and calculations.
6. Obtaining an operating simulation example;
7. Analysing, comparing and discussing the results obtained;
8. Reaching conclusions on the developed work, exposing the limitations and suggesting future work to be accomplished.

The intention of this document is to be written in a way that fosters a future comprehension of RDEs, the constraints associated, the significance of these kind of engines for the future of propulsion aviation systems, and the potential to continue conducting research in this matter. The dissertation strives to offer thorough explanations, transparent methodologies, and in-depth results, positioning itself as a valuable reference for those seeking insights in

this domain.

1.3 Dissertation Structure and Layout

This dissertation is divided into five Chapters. The first one is the introduction which includes the motivation, the objectives of the developed work, and the structure and layout of this dissertation.

The second Chapter includes the literature review where is presented a brief history of RDEs, how shock waves work, how combustion and how the detonation process works. It also presents valuable content about turbulence and CFD fundamentals.

The third Chapter presents the "Methodology" used to obtain the results. It includes the functioning of RDEs, a detailed description of the sizing process, boundary conditions and initialization. All the steps performed in ANSYS in order to run the simulation are presented and explained in this Chapter.

As for the fourth Chapter, it furnishes the simulation results stating all the calculations, figures, plots, and important calculated values. It also includes the analyses and discussion of the results obtained.

Lastly, the fifth Chapter reflects the developed work, challenges encountered, and potential enhancements for the study of RDEs and their usability in the future, delving into a more comprehensive analysis.

Chapter 2

Literature Review

This Chapter contains a literature review of some topics that are important to further understand the present work. It begins with a brief historical context of the birth of RDEs and their characterization.

It will also present what shock waves are and how they work. Similarly, how the combustion and detonation processes work will be explained and presented. Important insights about turbulence and CFD analysis will be given.

2.1 History of RDEs

Rotating detonation engines go back to the 1950's [4]. Professor James Arthur Nicholls at the University of Michigan was the first one to theorize detonative waves as a mean of producing thrust. He built and tested what is nowadays known as a pulse detonation engine (PDE) [5].

The PDE aims to tackle the power of detonations to propel a vehicle forward. The concept is: inject fuel and oxidizer, detonate, expel gases, repeat. The term "pulse" refers to the fact that these types of engines operate in a pulsed mode, so the thrust varies in time and the detonation must be initiated each time. To achieve nearly constant thrust they would probably operate at a frequency of at least 50 Hz [6]. The difference between a PDE and a RDE is that a RDE offers continuous thrust generation and can be applied basically to any Mach number [7].

Back in the 1960's, Professor Nicholls ran experiments aimed at discovering whether the rotating detonation wave was a feasible mean of propulsion for rockets. He was not able to get the engine run, but he believed it was possible. At that time, some properties of detonation were known, but researchers could not apply these properties in order to run these engines in a practical way [4].

Not being able to obtain the desired results, the Americans lost interest as other combustor designs progressed. On the other hand, the Soviet Union played a significant role in advancing research on detonation engines. Scientists like Valentin Dushin and Yuri Koryakin conducted experiments and developed theories related to rotating detonation. Their work laid the foundation for later research in the field.

After some decades, with natural gas power plants in vogue and conventional combustors

near their maximum efficiencies, the Americans gained interest again. In the mid-2000's, the Air Force Research Laboratories began publishing research on working rotating detonation engines [4]. NASA (National Aeronautics and Space Administration) and DARPA (Defense Advanced Research Projects Agency) have also been involved in funding research on RDEs.

Throughout the years, researchers from various institutions and countries (China, France, Japan, Poland, Russia, USA, and others) have been developing RDEs (Figure 2.1) and PDEs (Figure 2.2), conducting experiments for all kinds of possible configurations. "It is just only matter of time that the PDE and RDE will be utilized in the majority of jet propulsion systems" [7].

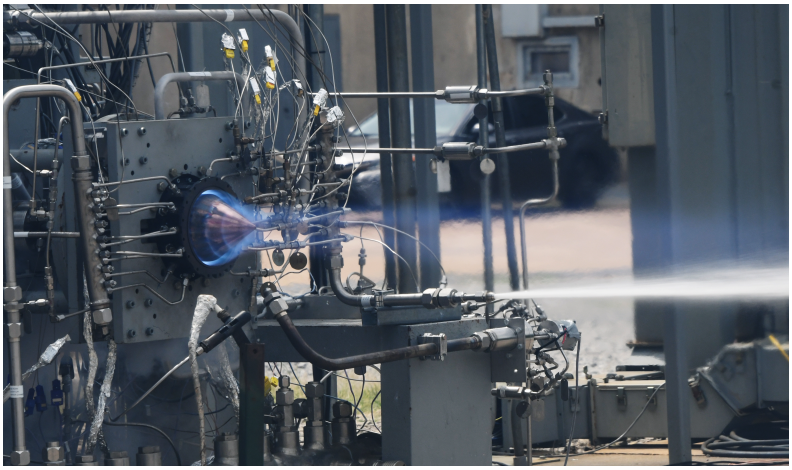

Figure 2.1: A prototype RDE under test at the Marshall Space Flight Centre. [8]

Figure 2.2: Air Force Research Laboratory PDE. [9]

2.2 Shock Waves

Shock waves are present in a range of different engineering application environments, for example, transonic gas turbine blade tip gaps, transonic blade passages, scramjet isolator ducts, supersonic aircraft engine intakes, adjacent to transonic and supersonic flight vehicle surfaces (see Figure 2.3), and nearby surfaces of rockets, missiles, and reentry vehicles [10].

A shock wave is a disturbance that travels at a speed surpassing the local speed of sound within a medium. Like a regular wave, it conveys energy and can move through a medium. However, it is distinguished by a sudden, almost abrupt alteration in the pressure, temperature, and density of the medium [11]. The energy and speed of a shock wave itself dissipate relatively quickly with distance. As a shock wave traverses through a substance, energy remains conserved, yet entropy rises. This transformation in the material's characteristics results in a reduction of extractable work energy and imposes a drag force on supersonic objects. Thus, shock waves represent highly irreversible processes [11].

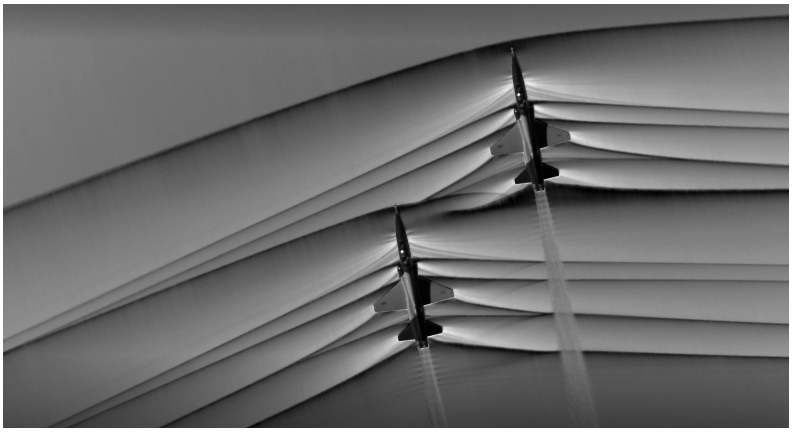

Figure 2.3: Schlieren photograph of an attached shock on a sharp-nosed supersonic body. [12]

When an object or disturbance surpasses the speed at which information can spread through the surrounding fluid, the fluid near the disturbance cannot respond or reposition itself before the disturbance reaches it. In a shock wave, the characteristics of the fluid, such as density, pressure, temperature, flow velocity, and Mach number, undergo nearly instantaneous changes (see Figure 2.4) [13]. Shock waves are exceptionally thin regions, usually much thinner than a sheet of paper. Studies measuring the thickness of shock waves in the air have yielded values of approximately 200 nanometers [14].

The more common shock waves are the normal (at 90° perpendicular to the shock medium's flow direction), the oblique (at an angle to the direction of flow), and the bow (occurs before the front of a blunt object when the incoming flow velocity exceeds Mach 1) [11].

2.2.1 Normal Shock

In the context of a steady flow, absence of body forces, and consistent cross-sectional areas before and after the shock, Equation 2.1 reflects flow continuity while considering compressibility effects. A normal shock is an extremely thin region marked by fluid properties discontinuity. Passing through normal shock results in increased pressure, density, and temperature, accompanied by a reduction in velocity to subsonic values [11] [14].

$$\rho_1 V_1 = \rho_2 V_2 \tag{2.1}$$

Once again, a shock is characterized by a discontinuity in fluid properties within an extremely thin region featuring significant temperature and pressure gradients. At the same time, viscosity and dissipative effects are strongly felt, making the process non-isentropic. However, since no heat is added or removed from the flow, the process is adiabatic [11] [14].

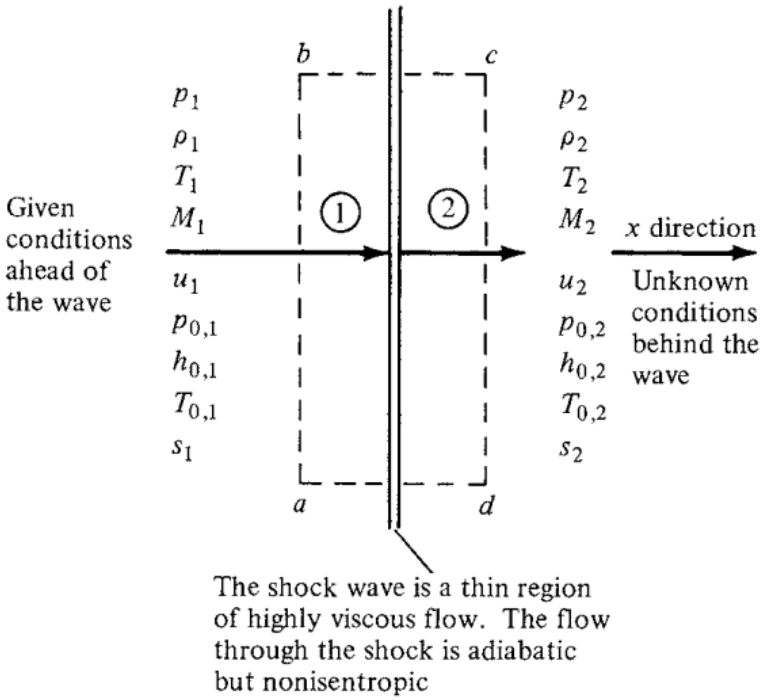

Figure 2.4: Sketch of a normal shock wave. [11]

Equations 2.2, 2.3, 2.4, 2.5, and 2.6 establish flow properties across the normal shock during an adiabatic and irreversible process.

$$M_2^2 = \frac{1 + \frac{\gamma-1}{2} M_1^2}{\gamma M_1^2 - \frac{\gamma-1}{2}} \tag{2.2}$$

$$\frac{p_{02}}{p_{01}} = \frac{\left(\frac{\frac{\gamma+1}{2}M_1^2}{1+\frac{\gamma-1}{2}M_1^2}\right)^{\frac{\gamma}{\gamma-1}}}{\left(\frac{2\gamma}{\gamma+1}M_1^2 - \frac{\gamma-1}{\gamma+1}\right)^{\frac{1}{\gamma-1}}} \tag{2.3}$$

$$\frac{\rho_2}{\rho_1} = \frac{(\gamma+1)\,M_1^2}{2+(\gamma-1)\,M_1^2} = \frac{V_1}{V_2} \tag{2.4}$$

$$\frac{p_2}{p_1} = 1 + \frac{2\gamma}{\gamma+1}\left(M_1^2 - 1\right) \tag{2.5}$$

$$\frac{T_2}{T_1} = \left(1 + \frac{2\gamma}{\gamma+1}\left(M_1^2 - 1\right)\right)\left(\frac{2+(\gamma-1)\,M_1^2}{(\gamma+1)\,M_1^2}\right) \tag{2.6}$$

While the equations acknowledge the possibility of subsonic flow before the shock (M<1), obedience to the second law of thermodynamics is crucial, Equation 2.7 reflects this consideration. For a unitary M, an isentropic infinitely weak normal shock, (s2 – s1 = 0), is achieved. Conversely, a subsonic M predicts a physically implausible negative entropy variation [11] [14].

$$s_2 - s_1 = c_p \ln\left(\frac{T_2}{T_1}\right) - R\ln\left(\frac{p_2}{p_1}\right) \tag{2.7}$$

As the process is adiabatic, the stagnation temperature remains constant. However, there is a drop in stagnation pressure, and its relation to entropy gain is expressed in Equation 2.8 [11] [14].

$$s_2 - s_1 = -R\ln\left(\frac{p_{02}}{p_{01}}\right) \tag{2.8}$$

2.2.2 Oblique Shock and Expansion Waves

In Subsection 2.2.1, shock waves that make an angle of 90° with the upstream flow were discussed. In general, a shock wave will make an oblique angle with respect to the upstream flow, named oblique shock wave. So, a normal shock wave is purely a specific case of the general family of oblique shocks. Additionally, to oblique shock waves, where the pressure increases discontinuously across the wave, supersonic flows are also characterized by oblique expansion waves, where the pressure decreases continuously across the wave [11].

Figure 2.5 illustrates oblique shocks and Figure 2.6 shows in detail the geometry of an oblique shock. They are formed when the flow is deflected at a certain angle, θ to the flow, due to

the presence of a concave surface. The streamlines are always parallel, changing direction discretely when the shock occurs.

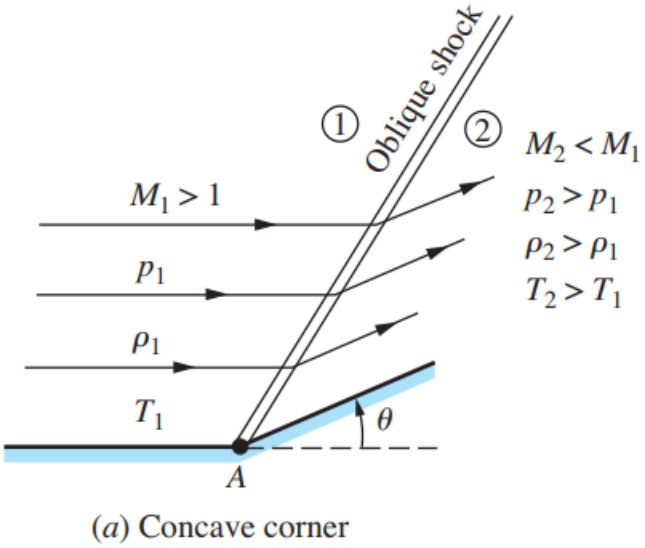

Figure 2.5: Supersonic flow over a concave corner. [11]

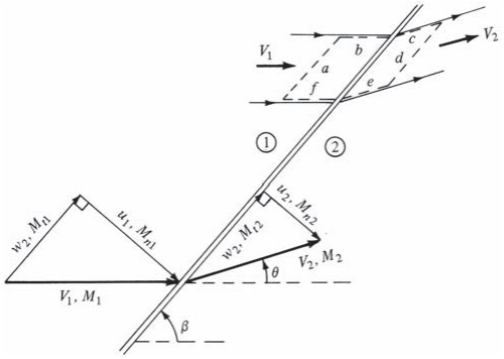

Figure 2.6: Detailed geometry of an oblique shock. [11]

To analyse an oblique shock the flow is decomposed into two components, one normal to the shock, which is analysed as a normal shock, and one parallel component that is not affected by the shock. Taking this into account we can use Equations 2.9, and 2.10.

$$M_{n,1} = M_1 \sin \beta \tag{2.9}$$

$$M_{t,1} = M_1 \cos \beta \tag{2.10}$$

In the equations above, β represents the shock angle that decomposes the velocity of the incoming flow, and θ represents the deviation experienced by the flow after the shock, coin-

ciding with the concavity of the surface.

The M after the shock can be calculated using Equation 2.11, and the relation between the angles mentioned before can be illustrated according to Equation 2.12.

$$M_2 = \frac{M_{2n}}{\sin(\beta - \theta)} \tag{2.11}$$

$$\tan\theta = \frac{2}{\tan\beta}\left[\frac{M_1^2 \sin^2\beta - 1}{M_1^2(\gamma + \cos 2\beta) + 2}\right] \tag{2.12}$$

Figure 2.7 represents graphically the relation between θ, β, and M.

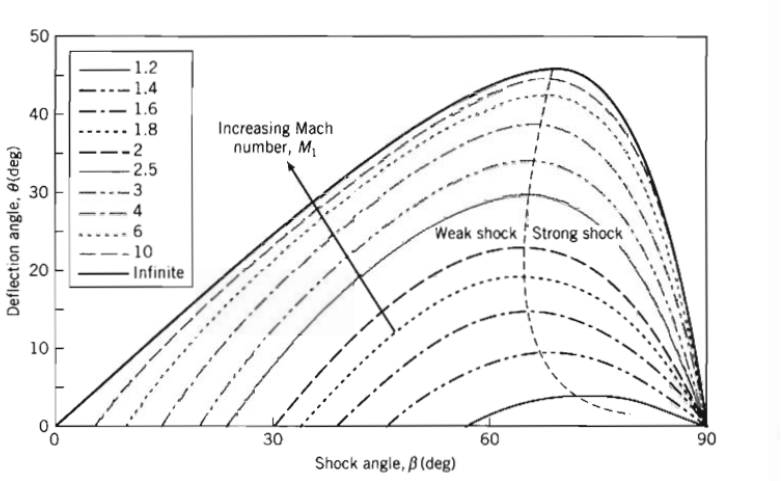

Figure 2.7: Relation between θ, β, and M. [14]

There exists a maximum angle, θ_{max}, to which the flow can be diverted by a straight oblique shock. If the surface has an angle θ greater than θ_{max}, the shock will curve, potentially leading to flow detachment. Similarly, when the deflection angle is constant, a decrease in the Mach number causes an increase in the shock angle until it reaches a point where the previously defined θ matches the maximum possible deflection angle θ_{max} for that Mach number. Beyond this point, further reductions in the Mach number do not yield a straight shock solution [11] [14].

For a given deflection angle, two potential shock wave angles exist. The smaller angle aligns with the weak shock solution, where the post-shock flow remains supersonic ($M_2 > 1$). Conversely, the larger angle corresponds to the strong shock solution, resulting in subsonic post-shock flow ($M_2 < 1$). The determination of each solution hinges on the downstream pressure conditions relative to the pre-shock flow. A robust pressure gradient promotes the strong shock solution, whereas a more subdued gradient favors the weak shock solution [11] [14].

When a supersonic flow encounters a convex surface, it undergoes deflection, resulting in an expansion rather than an oblique shock. In this scenario, velocity increases, while density, pressure, and temperature decrease. These property changes exhibit so smoothly, that a continuous behaviour can be assumed, linking to an isentropic process. This smooth transition is facilitated by the expansion, which is formed by a fan of waves, each incrementally contributing to the acceleration of the flow [11].

Figure 2.8 presents an illustration of expansion waves.

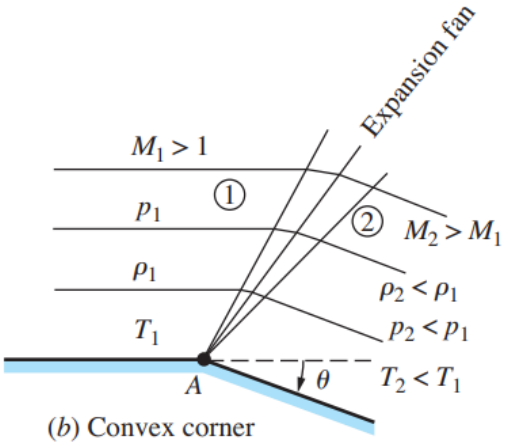

Figure 2.8: Supersonic flow over a convex corner. [11]

The vertex A in Figure 2.8 is the origin of the generation of infinitesimal Mach lines that emanate from it and expand the flow. These Mach lines are characteristic, with consistent properties between them.

Owing to the isentropic nature of the process, temperature and pressure alterations in the flow are governed by Equations 2.13, and 2.14, respectively.

$$\frac{T_2}{T_1} = \frac{1 + \frac{\gamma-1}{2} M_1^2}{1 + \frac{\gamma-1}{2} M_2^2} \tag{2.13}$$

$$\frac{p_2}{p_1} = \left(\frac{1 + \frac{\gamma-1}{2} M_1^2}{1 + \frac{\gamma-1}{2} M_2^2} \right)^{\frac{\gamma}{\gamma-1}} \tag{2.14}$$

The Prandtl-Meyer angle is defined by Equation 2.15 for a specific Mach. Concerning the reflection angle, it is simply the difference between the Prandtl-Meyer angle before and after the expansion, as outlined in Equation 2.16.

$$\nu(M) = \sqrt{\frac{\gamma+1}{\gamma-1}}\tan^{-1}\sqrt{\frac{\gamma-1}{\gamma+1}(M^2-1)} - \tan^{-1}\sqrt{M^2-1} \tag{2.15}$$

$$\theta = \nu(M_2) - \nu(M_1) \tag{2.16}$$

2.2.3 Detonation Waves

At the beginning of investigations, about 140 years ago, detonation waves (DWs) were considered as plane waves without any internal structure. Many years later, it came as a surprise when the unusual regimes of detonation wave propagation in tubes of round cross-sections with spiral trajectories were observed by researchers in 1927. This regime was called the spinning DW. Professor B. Voitsekhovsky was the first one to identify the structure of a spinning DW [15].

A detonation wave is essentially a shock followed by a chemical reaction, and it propagates at supersonic speeds. It is highly three-dimensional, and its structure is extremely complicated. It involves a wave traveling through a highly combustible or chemically unstable medium. The chemical reaction of the medium will faithfully follow the shock, and the chemical energy of the reaction drives the wave forward.

A DW behaves distinctively from a conventional shock wave, primarily because it is propelled by the chemical reaction taking place behind its shock wavefront. According to the basic theory of detonations, an unsupported and self-sustaining detonation wave moves at the Chapman-Jouguet flow velocity. Additionally, the detonation event induces overpressure, leading to the propagation of a shock wave into the surrounding air.

The Chapman–Jouguet condition is approximately valid for detonation waves in high explosives. It asserts that the detonation advances at a velocity where the reacting gases just attain sonic velocity (in the frame of the leading shock wave) as the chemical reaction concludes. Originally formulated in 1900 for an infinitesimally thin detonation, the condition finds its physical interpretation in a later model developed around 1943. This model, known as the ZND (Zel'dovich - von Neumann - Döring) detonation model, provides a more comprehensive understanding of the Chapman–Jouguet condition [16].

The ZND detonation model is an idealized one-dimensional model that illustrates gaseous detonations. The model begins with the initiation of a detonation by a shock wave, leading to a compressed and heated region. In the reaction zone, chemical reactions occur rapidly, transforming reactants into products. This zone is often considered to be a thin layer compared to the overall wave structure. The detonation wave propagates at a velocity where the

reacting gases just reach sonic velocity as the reaction ceases (Chapman–Jouguet condition). The model describes a front where the transition from reactants to products occurs, energy is released, sustaining the detonation wave. It assumes a quasi-steady-state, allowing for the decoupling of the various stages of the detonation process. This simplification facilitates mathematical analysis [17].

Figure 2.9 shows a diagram of this idealized one-dimensional model.

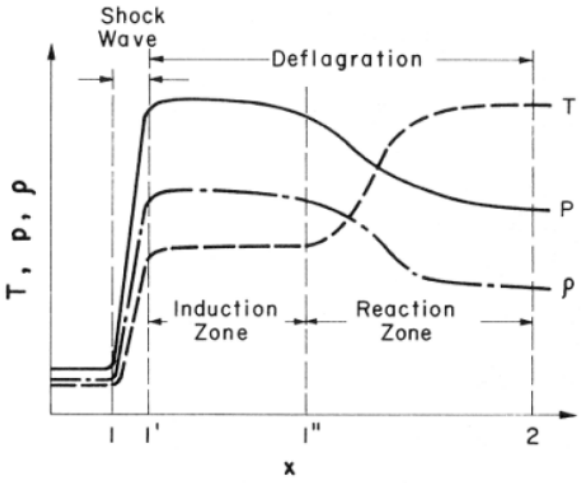

Figure 2.9: Diagram of a ZND Detonation Wave. [18]

2.3 Combustion

Throughout history, the phenomena of combustion, fire, and flame have captivated civilizations, each developing its own interpretations. The ancient Greeks conceptualized combustion through philosophical doctrines, proposing the existence of an ”inflammable principle” released during burning.

In the early 17th century, Sir Francis Bacon and others made key observations about candle flames and air’s role in combustion. German physicist Otto von Guericke demonstrated that air’s absence hindered combustion, while Robert Hooke suggested an active component in air combining with combustibles to create flame. Antoine-Laurent Lavoisier, in 1772, made a groundbreaking contribution by asserting that burned substances gained weight due to combining with air. He identified this crucial element as ”oxygen,” setting the stage for a modern understanding of combustion [19].

Lavoisier’s theory, grounded in the conservation of matter and the concept of elements, marked a paradigm shift in chemistry. John Dalton’s, an English chemist, work on gases, along with advancements in measuring atomic weights, strengthened Lavoisier’s theory. Discoveries of nitrogen, hydrogen, carbon dioxide, and carbon monoxide in the late 18th century further supported this revolutionary approach to chemistry [19].

In the early 19th century, Sir Humphry Davy delved into combustion, measuring flame temperatures, and uncovering catalytic combustion. However, despite these strides, a comprehensive understanding of energy's role in combustion remained elusive until Sir Benjamin Thompson's 1798 experiments highlighted heat as a particle movement [19].

The 19th century witnessed the development of the kinetic theory of gases, thermodynamics, and thermochemistry, shedding light on the energy aspects of combustion. Further investigations into burning velocities, gas mixture combustion, and thermal dissociation refined combustion mechanism theories. The study of flame-emitted light, through the spectroscope and spectral analysis, deepened our understanding of flame nature. Industrial progress, particularly in addressing explosion hazards in coal mines, spurred research into flame phenomena [19].

By 1881, the discovery of detonation paved the way for a detonation theory in the early 20th century, treating gases as fluids under certain conditions. Post-1930s, chemical kinetics became integral to flame propagation theory, marking significant progress in comprehending combustion mechanisms [19].

2.3.1 Combustion Fundamentals

To propel an airplane or a model rocket through the air, a propulsion system is essential to generate thrust. Various types of aircraft employ different propulsion devices, but all rely on engines to produce power. Whether it is rocket engines, internal combustion, piston engines, or jet engines, the common factor is the combustion of fuel to generate power.

Combustion, at its core, is an exothermic chemical process wherein a substance reacts rapidly with oxygen, releasing heat in the process. The initial substance involved is termed the fuel, while the provider of oxygen is known as the oxidizer. Fuels can exist in solid, liquid, or gas forms, with liquid being the prevalent choice for airplane propulsion. Similarly, oxidizers may be solid, liquid, or gas, but in aviation, gases (such as air) are commonly used. Model rockets, on the other hand, typically utilize solid fuel and oxidizer combinations [20]. The rate at which the reactants combine is high because of the nature of the chemical reaction itself, and because more energy is generated than can escape into the surrounding medium. This results in a rise in the temperature of the reactants, accelerating the reaction even more [19].

One familiar example of a combustion reaction is a lighted match. When a match is struck, the friction generates enough heat at the match head, initiating a chemical reaction that produces more heat, leading to the ignition of a flame. If external factors, such as wind or moisture, interfere with the heat transfer or chemical reactions, the match may fail to ignite. Assuming successful ignition, the flame's heat raises the temperature of the nearby matchstick layer and surrounding oxygen, prompting a combustion reaction between the wood and oxygen. Combustion ceases when equilibrium is reached, balancing the total heat energies

of reactants and products, which includes emitted heat and light. Flames exhibit a distinct composition and intricate structure, characterized as multiform, capable of existing at both low and extremely high temperatures. The emission of light within the flame stems from the presence of excited particles, charged atoms and molecules, and electrons [19].

Types of Combustion

There are essentially five different types of combustion, named complete combustion, incomplete combustion, rapid combustion, spontaneous combustion, and explosion [21].

Complete combustion occurs when an unlimited supply of air or oxygen exists. An exothermic reaction between the oxygen, and the carbon and hydrogen atoms of a hydrocarbon fuel occurs. The hydrocarbon will burn completely and leave only two products (water and carbon dioxide). One example of this is when a candle burns, the heat from the wick will vaporize the wax which reacts with the oxygen in the air, and in an ideal situation all the wax burns up and complete combustion takes place [21].

Incomplete combustion occurs when there is a limited supply of air or oxygen. When compared with a complete combustion, less energy is emitted in this reaction, and although there is still water in the products, there is also carbon monoxide and carbon because one part of the fuel did not react completely [21].

Rapid combustion, and sometimes called fast combustion takes place when a substance burns rapidly and produces heat and flame, usually achieved by introducing external heat. Substances that have lower ignition temperatures, such as liquefied petroleum gas, compressed natural gas, and petrol, experience this type of combustion [21].

Spontaneous combustion happens when suddenly a substance starts turning into flame without the supply of any external cause such as heating. Substances having a relatively low ignition temperature generally burn by this type of combustion. Examples of spontaneous combustion are Phosphorus and Sulphur start burning instantaneously at room temperature, haystacks, linseed oil, coal, and pyrite sometimes start burning suddenly with flame because of a temperature increase. Also, in coal mines, fire breaks out many times due to the combustion of coal dust, and in forests, fire often breaks out due to an increase in temperature caused by the sun [21].

Explosive combustion happens when the reaction occurs very rapidly. An explosion is a sudden, rapid release of energy that produces potentially damaging pressures. The reaction occurs when something ignites to produce heat, light, and sound energy [22].

Gaseous fuels, when reaching a specific air-fuel concentration, can form an explosive atmosphere. The introduction of an ignition source in this environment results in the creation of a flame that travels away, expanding the burned gases. In confined spaces, the explosion leads

to increased pressure upon rupture, commonly associated with the term ”explosion.” However, explosions can occur without confinement, as the rapid flame speed generates compression waves capable of causing damage. The extent of damage depends on the pressure and the speed of energy release, with explosions categorized as either detonations or deflagrations based on their flame speed [22]. In Section 2.4 there is a detailed explanation of the difference between deflagration and detonation.

2.4 Detonation versus Deflagration

Combustion processes have been recognized for over a century to occur in two distinct modes: deflagration and detonation. The description of the detonation process dates to 1881. Nearly two decades later, was independently presented the zero-dimensional theory of detonation, a concept now widely discussed in combustion literature [23].

In deflagration, a combustion wave moves with subsonic velocity, resulting in a decrease in pressure and density. On the other hand, detonation produces a strong shock wave followed by a reaction front moving at sonic velocity. In detonation, the final products exhibit higher density and pressure than the initial mixture. Despite both processes leading to significantly higher temperatures in the combustion products compared to the initial mixture, the maximum temperatures differ between deflagration and detonation. For the same mixture composition, the maximum temperatures in detonation are higher than those in deflagrative combustion [2] [23].

Distinct differences also exist in the velocity of the combustion waves. Deflagration features a reaction front velocity ranging from centimeters per second in laminar flames to meters per second in turbulent flames. In contrast, a detonation front in gaseous or hybrid mixtures always propagates at velocities of kilometers per second [2]. Initiating detonation requires much higher energy than initiating deflagration, and the detonation process can also be self-accelerated in long channels or tubes [23].

Given the variation in product parameters depending on whether combustion exhibits a deflagrative or detonative nature, applying different combustion modes to a propulsion system can result in distinct system performance. Figure 2.10 provides a comparison of ideal thermodynamic cycles for different combustion processes applied in an engine.

Combustion initiates at point 2 for all cases. In the isobaric Brayton cycle, the addition of heat (involving deflagrative combustion) leads to an increase of volume. It’s important to note that, in the practical scenario of deflagration, there is a slight decrease in pressure. Conversely, in the isochoric case pressure increases because of constant volume heat addition, implying constant volume combustion. The heat addition on the detonation mode, represented by the Fickett-Jacobs cycle, results in the highest pressure increase and a decrease in specific volume.

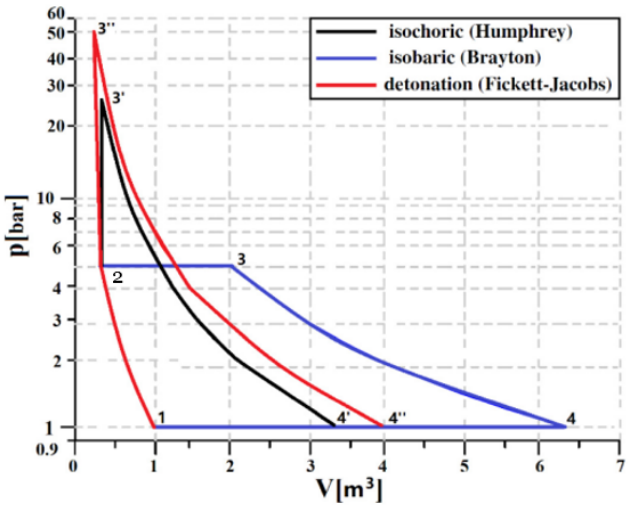

Figure 2.10: Comparison of thermodynamic Humphrey, Brayton, and Fickett-Jacobs cycles. [2]

Equations 2.17, 2.18, and 2.19 describe the efficiency of the Brayton, Humphrey, and Fickett-Jacobs cycles, respectively.

$$\eta_B = 1 - \frac{1}{\left(\frac{p_2}{p_1}\right)^{\frac{\gamma-1}{\gamma}}} \tag{2.17}$$

$$\eta_H = 1 - \gamma \frac{T_1}{T_2} \frac{\left(\frac{T_{3'}}{T_2}\right)^{\frac{1}{\gamma}} - 1}{\left(\frac{T_{3'}}{T_2}\right) - 1} \tag{2.18}$$

$$\eta_F = 1 - \gamma \frac{1}{\left(\frac{p_2}{p_1}\right)^{\frac{\gamma-1}{\gamma}}} \frac{\left(\frac{T_{3''}}{T_2}\right)^{\frac{1}{\gamma}} - 1}{\left(\frac{T_{3''}}{T_2}\right) - 1} \tag{2.19}$$

Comparison of calculated efficiency for the three different thermodynamic cycles for an initial compression ratio constant, show that the highest efficiency will be obtained for the detonation (Fickett-Jacobs) cycle, considering the initial compression process (1-2 in Figure 2.10) the same for all cycles. The efficiency of the cycle increases more than 20% [23].

This potential for a substantial enhancement in cycle efficiency serves as a primary driver for researching the implementation of detonative combustion in propulsion systems. However, this motivation is not singular. The simpler design, the fact that the detonation velocity is on

the order of km/s, implying a short combustion zone and a more compact chamber, the lower NOx emissions, and no need to mix extra air, and the increase of pressure due to detonation are very important factors and advantages when compared to deflagration [2] [23].

2.5 Detonation Engines

Various methods exist for implementing detonative combustion in propulsion systems, offering a spectrum of operational possibilities. In engines, detonation can be either stationary concerning the engine frame, stationary or quasi-stationary concerning a moving coordinate system, transient with parameters varying during engine operation, or pulsating in nature [23].

The application of stationary detonation is linked to the concept of an engine featuring a standing detonation wave. On the other hand, quasi-stationary detonation propulsion, which is stationary relative to the rotating frame of reference, is associated with RDEs. PDEs utilize flame acceleration to achieve detonation in specially designed tubes [23].

All engines based on detonative combustion provide advantages such as a higher rate of energy release, increased thermodynamic efficiency, and a more compact heat release chamber compared to conventional engines using deflagration [7].

Figure 2.11 shows the theoretical dependence of specific impulse on flight Mach number for different propulsion systems and different fuels.

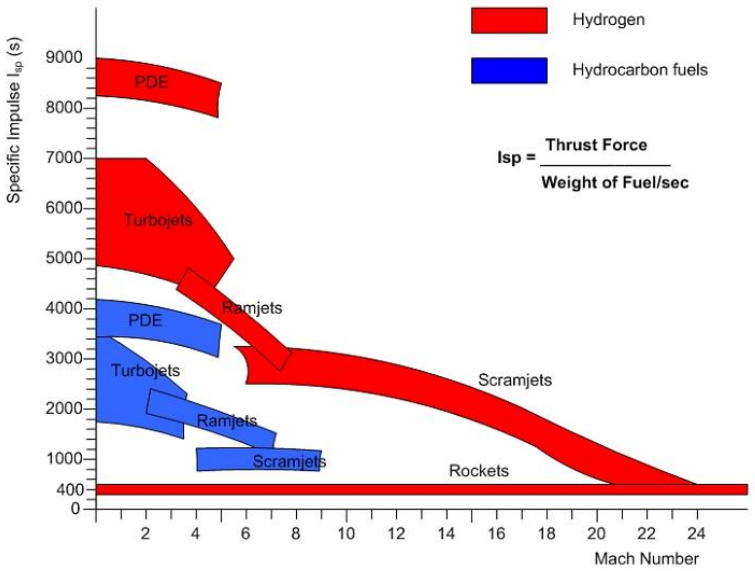

Figure 2.11: Mach Number versus Specific Impulse for various propulsion systems. [24]

The specific Impulse, I_{sp}, is directly related to how efficient the propulsion system produces thrust from the propellant mass leaving the vehicle. The higher the I_{sp}, the less propellant

mass needed to produce the same thrust or the higher the exhaust velocity [25]. As Figure 2.11 shows, the I_{sp} for PDEs propulsion systems is much higher than for other conventional engines.

Again, this gives strong motivation to apply detonative combustion to jet engines. Three types of jet engines can utilize detonation for energy release in engine combustion chamber, and they will be discussed in the next Subsections.

2.5.1 Pulsed Detonation Engine (PDE)

A Pulse Detonation Engine (PDE) typically comprises a sufficiently long tube filled with fresh fuel-oxidizer mixtures, ignited by a strong energy source. The flame initiated by ignition must rapidly accelerate to detonation velocity over a short distance, transitioning from deflagration to detonation. The detonative combustion produces high pressure, which is then converted into thrust. After the entire mixture is consumed by detonation, combustion products are evacuated from the tube, fresh mixture quickly replenished, and the cycle repeats. The typical operational frequency of such engines is usually in the range of a dozen Hertz [7].

PDEs can operate across a wide range of flight Mach numbers, spanning from zero up to M4+. However, the engine operates in a pulsed mode, causing time-varying thrust as detonation must be initiated at each cycle. The system is complex due to the need for rapid purging and refilling. Additionally, the engine operates under stoichiometric conditions (necessary for fast initiation of detonation), and the frequency is relatively low. If pulsed detonation were to be applied to turbojet combustion chambers, it would be essential to introduce extra air to reduce temperature before the first turbine stage [7].

Figure 2.12 shows the first PDE designed by Professor Nicholls at University of Michigan, and Figure 2.13 shows the operating principle of the PDE.

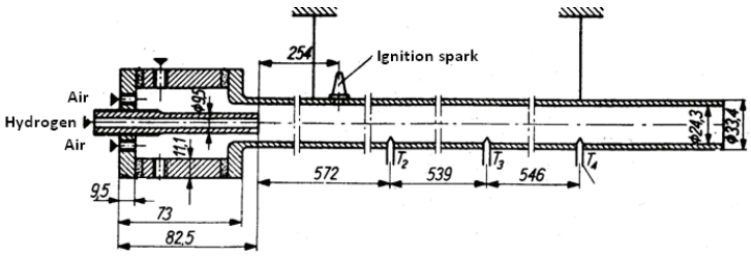

Figure 2.12: First PDE designed by J. A. Nicholls at the University of Michigan. [26]

The PDE cycle begins with the injection of a fresh mixture into the tube (t1). Once the mixture is introduced, the opening at the tube entry is sealed, initiating a detonation (t2). As the detonation propagates within the tube, rarefaction waves are generated, exerting pressure on the closing plate of the tube generating thrust force (t3). After a certain duration, the pressure front reaches the end of the tube (t4), initiating the exhaust of the detonation products (t5). This continues until most products are expelled, and the pressure drops below

the surrounding pressure (t6), completing the cycle and allowing for the initiation of a new one. In practical implementation, the process deviates from this ideal model [23].

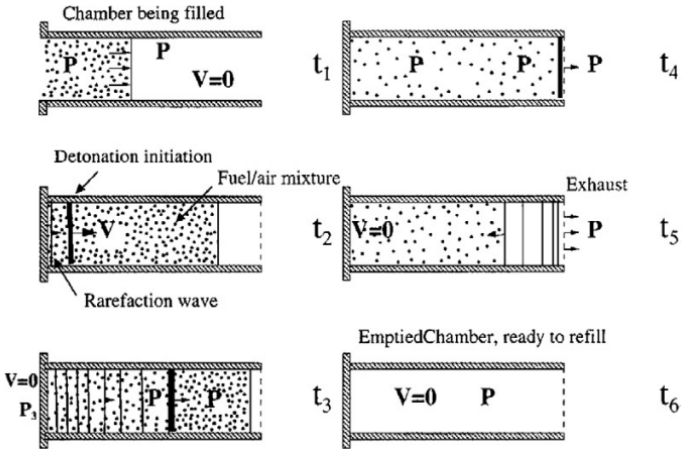

Figure 2.13: Operating principle of the PDE. [27]

While the incorporation of PDEs into practical applications is expected to take time, a significant goal was achieved in January 2008 at the Mojave Air and Space Port. During an experimental flight, an aircraft equipped with a PDE took off and landed using a conventional turbojet engine. The PDE was activated for 10 seconds during flight, marking the historic event of being the first authentic application of such an engine in an aerospace flight vehicle. This pioneering flight raises hopes for future applications of PDE technology [23].

2.5.2 Standing Detonation Engine (SDE)

The way this engine operates is relatively simple. Figure 2.14 shows a schematic diagram of this type of engine. The fuel is injected into supersonic flow, and by wedge or other ways, the detonation wave is stabilized inside the engine, and the products are expanding inside the nozzle [7].

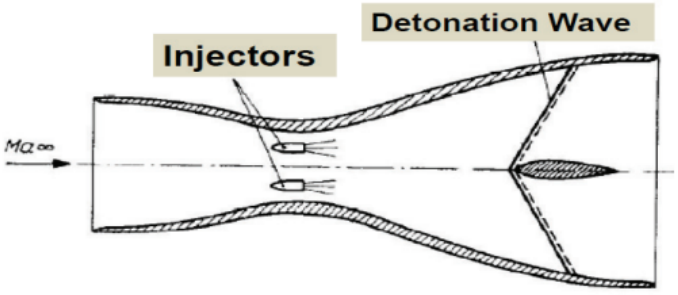

Figure 2.14: Schematic diagram of the SDE. [28]

Numerical modeling of the stability and performance of this engine shows some major disadvantages. The fact that it could be only used for a very limited range of flight velocity. The lower limit of engine operation is basically the Chapman–Jouguet detonation velocity, but

the upper limit is somewhere in the range of Mach number 7–8. For higher M, the aerodynamic forces applied for an engine with a conical outside envelope will start to produce higher drag than the propulsive force. For this reason, a standing detonation wave engine could only be applied for steady flight velocities with Mach numbers in the range of 5– 7, so it could have very limited, if any, applications [23].

2.5.3 Rotating Detonation Engine (RDE)

The Rotating Detonation Engine functions as a thrust-generating device where self-sustained combustion-driven shock waves, or detonations, travel azimuthally within an annular combustion chamber. Unlike conventional engines relying on deflagration, the detonation process in a RDE leads to a rise in pressure. The successful application of 'pressure gain' combustion implies simplification in the mechanical aspects of propulsion systems, such as reduced pumping requirements for propellant. This, in turn, results in an increased availability of work for a given propellant compared to conventional engines, ultimately leading to fuel savings. However, RDEs exhibit a range of experimentally observed instabilities and bifurcations, which are widespread and may potentially impact performance and stable operation. Despite these complications it is worthy to continue doing research on this matter, since it brings many advantages that may revolutionize the world of propulsion as we know it today. [29]

The principle of RDEs is based on the formation of continuously propagating detonation in a disk-like combustion chamber (toroidal or ring-like shape). Air (or oxygen) is supplied through a narrow slit at critical conditions and fuel is injected through several small holes. Initiator and pressure transducer are placed on the outside wall of the cylindrical detonation chamber. Such chamber can be applied to different kinds of jet engines, such as: turbojet or gas turbine, ramjet, or rocket [7]. Figure 2.15 shows a schematic diagram of the detonation chamber and Figure 2.16 shows the typical pressure measurements.

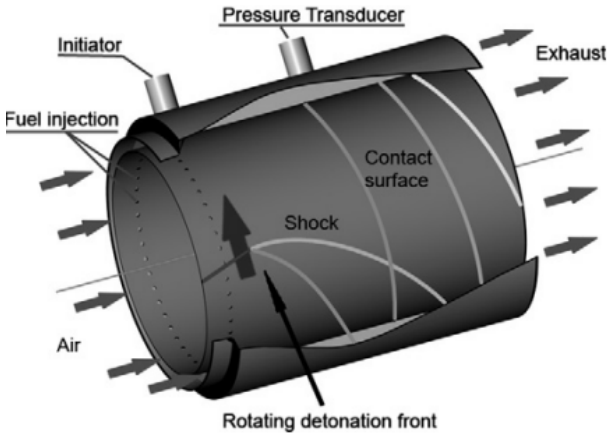

Figure 2.15: Schematic diagram of a detonation chamber. [30]

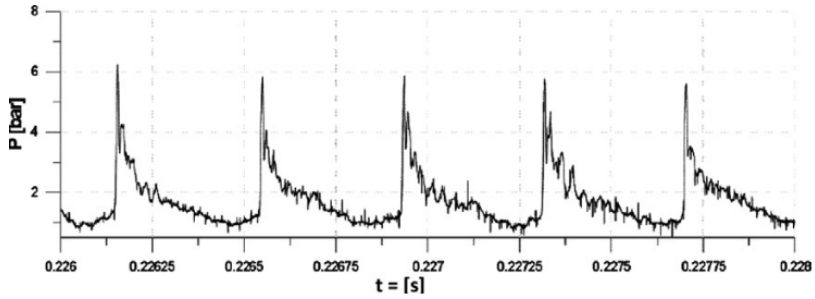

Figure 2.16: Typical pressure variation for detonation in research chamber. [23]

The most basic application of a continuously rotating detonation is the rocket engine. In this engine design, fuel and oxidizer are injected into a cylindrical detonation chamber, sustaining a continuous rotating detonation wave as long as the chamber is supplied with fuel and oxygen. As the products exit the detonation chamber at supersonic velocities, the conventional need for a diverging-converging nozzle is eliminated, and an aerospike nozzle can be directly attached to the detonation chamber. A small-scale model of this rocket engine was tested at Warsaw University of Technology, operating with various gaseous oxygen-fuel mixtures. Fuels such as hydrogen, methane, ethane, and propane were utilized. While rotating detonation was achieved for all mixtures, a comprehensive thrust measurement was specifically conducted for the methane-oxygen mixture. [7]

In the application of continuously rotating detonation in various jet engines, including supersonic ramjet engines and turbojets, the detonation can be organized in a special subchamber, where a rich fuel-air mixture undergoes detonation, or within the entire cross-section behind the normal shock wave. In either scenario, the engine's length is significantly reduced compared to conventional ramjets. Successful laboratory operation of a ramjet with a rotating detonation engine (RDE) in ejection mode has been reported [31].

The application of the continuously rotating detonation combustion process in all jet engines offers advantages such as a compact combustion chamber, resulting in shorter, simpler engines with higher performance due to pressure increase in detonative combustion. RDEs are expected to have lower mass and cost-effectiveness, and they contribute to environmental friendliness, because rotating detonation can be organized for lean mixtures, leading to reduced pollutant emissions and, in the case of hydrogen as fuel, potentially no CO_2 emissions. [7]

A combined cycle with a RDE is also feasible, which may be suitable for supersonic transport planes. This configuration allows for initial acceleration in rocket mode, transitioning gradually to ramjet mode for cruising. The initial need for liquid oxidizer during the rocket mode increases the takeoff mass but is later compensated by the lower mass of ramjet engines compared to complex turbo-rocket engines. Throughout cruising at supersonic velocities, engines operate in the ramjet RDE mode. [7]

RDEs have diverse applications, ranging from commercial aircraft to supersonic transport and rocket propulsion. In Poland, research on RDEs is conducted at the Institute of Heat Engineering, Warsaw University of Technology (WUT), and the Institute of Aviation. WUT achieved rotating detonation for various mixtures and geometries, while the Institute of Aviation is working on applying rotating detonation to the GTD-350 helicopter engine, with testing expected in two years. [7] [23]

2.6 CFD Fundamentals

CFD can be described as the science of predicting fluid flow behaviour and how it influences processes such as heat transfer, mass transfer, chemical reactions, and related phenomena, using computer-based simulations. It involves using computers to solve the mathematical equations governing fluid flow and heat transfer processes, such as the Navier-Stokes equations, conservation of mass, and conservation of energy equations [32]. It allows engineers and scientists to design or improve products and processes without the need for expensive and time-consuming physical prototypes.

CFD simulations vary from basic 2D simulations to much more challenging 3D analyses involving multiphase flows, turbulence, combustion, and beyond. Despite offering many advantages such as cost-effectiveness, efficiency, and flexibility over experimental techniques, we must keep in mind that CFD demands meticulous validation and verification to guarantee the precision and trustworthiness of the outcomes [32].

2.6.1 Governing Flow Equations

The goal of a CFD simulation is to solve a physical problem by obeying certain governing equations. These equations describe the physical properties of the fluid motion and represent the mathematical statements of three fundamental physical principles upon which all of fluid dynamics is based (mass is conserved, Newton's second law and energy is conserved) [33].

There are different flow models, such as fixed or moving finite control volume, and fixed or moving infinitesimally small volume. Each different flow model directly produces a different mathematical statement of the governing equations, some in conservation form and others in non-conservation form. These mathematical equations embody physical principles namely, the continuity, momentum, and energy equation, also known as Navier-Stokes equations. The set of equations becomes complete with the addition of the equation of state, and the terms to account for the effects of the chemical reactions [33] [34].

Having said that, the governing equations for an unsteady, three-dimensional, compressible, viscous flow will be presented next.

Continuity Equation

Applying the fundamental physical principle of mass conservation (matter may neither be created nor destroyed), meaning that the rate of change of mass within an arbitrary control volume must be equal to the total mass flow over its boundaries it is possible to reach to the mass conservation or continuity equation:

$$\frac{\partial \rho}{\partial t} + \frac{\partial (\rho u)}{\partial x} + \frac{\partial (\rho v)}{\partial y} + \frac{\partial (\rho w)}{\partial z} = 0 \tag{2.20}$$

$$\frac{\partial \rho}{\partial t} + \nabla \cdot (\rho \mathbf{V}) = 0 \tag{2.21}$$

In Equation 2.21, the left term corresponds to the rate of change in time of the density (mass per unit volume), and the second term is the net flow of mass out of the element across its boundaries, normally called the convective term. The bold format stands for vector notation [33] [34].

Momentum Equation

Newton's second law states that the rate of change of momentum of a fluid particle equals the sum of the forces on the particle. These forces are distinguished into two different types, surface forces (pressure forces, viscous forces, gravity force) and body forces (centrifugal force, Coriolis force, electromagnetic force) [33].

$$\frac{\partial (\rho u)}{\partial t} + \nabla \cdot (\rho u \mathbf{V}) = -\frac{\partial p}{\partial x} + \frac{\partial \tau_{xx}}{\partial x} + \frac{\partial \tau_{yx}}{\partial y} + \frac{\partial \tau_{zx}}{\partial z} + \rho f_x \tag{2.22}$$

$$\frac{\partial (\rho v)}{\partial t} + \nabla \cdot (\rho v \mathbf{V}) = -\frac{\partial p}{\partial y} + \frac{\partial \tau_{xy}}{\partial x} + \frac{\partial \tau_{yy}}{\partial y} + \frac{\partial \tau_{zy}}{\partial z} + \rho f_y \tag{2.23}$$

$$\frac{\partial (\rho w)}{\partial t} + \nabla \cdot (\rho w \mathbf{V}) = -\frac{\partial p}{\partial z} + \frac{\partial \tau_{xz}}{\partial x} + \frac{\partial \tau_{yz}}{\partial y} + \frac{\partial \tau_{zz}}{\partial z} + \rho f_z \tag{2.24}$$

Equations 2.22, 2.23, and 2.24 represent the momentum equation in the x, y, z components,

respectively. The terms on the left-hand side of the equations represent the rates of increase of x, y and z momentum. The right-hand side represents the normal stress due to the pressure (first fraction), the viscous stresses (second, third and fourth fractions), and the effects of the body forces (last term).

Energy Equation

The energy equation, rooted in the first law of thermodynamics, governs the conservation of energy within a fluid element. It states that changes in the total energy of the fluid over time are influenced by two main factors: the heat entering or leaving the element and the work done on it by external forces.

$$\begin{aligned}\frac{\partial}{\partial t}\left[\rho\left(e+\frac{V^2}{2}\right)\right]+\nabla\cdot\left[\rho\left(e+\frac{V^2}{2}\right)\mathbf{V}\right] &= \rho\dot{q}+\frac{\partial}{\partial x}\left(\kappa\frac{\partial T}{\partial x}\right)+\frac{\partial}{\partial y}\left(\kappa\frac{\partial T}{\partial y}\right)+\frac{\partial}{\partial z}\left(\kappa\frac{\partial T}{\partial z}\right)\\ &\quad -\frac{\partial\left(up\right)}{\partial x}-\frac{\partial\left(vp\right)}{\partial y}-\frac{\partial\left(wp\right)}{\partial z}\\ &\quad +\frac{\partial\left(u\tau_{xx}\right)}{\partial x}+\frac{\partial\left(u\tau_{yx}\right)}{\partial y}+\frac{\partial\left(u\tau_{zx}\right)}{\partial z}\\ &\quad +\frac{\partial\left(v\tau_{xy}\right)}{\partial x}+\frac{\partial\left(v\tau_{yy}\right)}{\partial y}+\frac{\partial\left(v\tau_{zy}\right)}{\partial z}\\ &\quad +\frac{\partial\left(w\tau_{xz}\right)}{\partial x}+\frac{\partial\left(w\tau_{yz}\right)}{\partial y}+\frac{\partial\left(w\tau_{zz}\right)}{\partial z}+\rho\mathbf{f}\cdot\mathbf{V}\end{aligned} \tag{2.25}$$

$$\dot{q}_j=-\kappa\frac{\partial T}{\partial j} \tag{2.26}$$

Thus, Equation 2.25 is the conservation form of the energy equation, written in terms of the total energy, $e+\frac{V^2}{2}$, which is the sum of internal energy and kinetic energy per unit mass. This equation represents the rate of change of energy inside a fluid element equal to the net flux of heat into the element plus the rate of work done on the element due to body and surface forces [33].

As we can imagine, for complex fluid flow problems, analytical solutions of governing equations are often impractical, necessitating numerical methods for acquiring a solution. Among these, the finite volume method, especially prominent in CFD, is widely used. The finite volume method involves discretizing the fluid domain into small sub-volumes or cells, forming a computational mesh. This mesh serves as the basis for locally solving discretized governing equations. Time is also discretized into intervals known as time steps, crucial for transient

simulations where solutions evolve over time. Once the domain is discretized, the governing equations are integrated over each control volume, yielding algebraic equations for discrete variables. These equations are then linearized and solved iteratively to update the variables at each time step. In essence, the finite volume method breaks down the problem into manageable elements, facilitating a numerical solution through a step-by-step iterative process [32] [34].

2.6.2 Turbulence and Turbulence Models

Turbulence is the apparent chaotic motion of fluid flows. Fluid flows can be laminar when they are regular and flow in an orderly manner. When the speed or characteristic length of the flow is increased, the convective forces in the flow overcome the viscous forces of the fluid, and the laminar flow transitions into a turbulent one. The ratio between convective and viscous forces is called the Reynolds number which is given by Equation 2.27. As the Reynolds number increases, the development of a laminar flow into a turbulent flow becomes more likely, being a higher Reynolds number an indicative of a more turbulent flow [35] [36].

$$Re = \frac{\rho V L}{\mu} \tag{2.27}$$

Furthermore, turbulent flows are characterized by the presence of eddies with a wide range of lengths that have complex and dynamic interactions. These eddies create large fluctuations in velocity and other properties which make them very difficult to predict or analyse. Figure 2.17 shows velocity fluctuations for steady laminar and turbulent flow [35].

Reynolds' decomposition states that the value of a velocity component at a certain point is the sum of its average value and a fluctuation that is a function of time, as seen in Equation 2.28. It is important to note that turbulent motion is random, and therefore a statistical treatment is essential [36].

$$v\left(t\right) = \bar{v} + v'\left(t\right) \tag{2.28}$$

In essence, turbulent flow is characterized by its irregularity, high diffusion, and dissipation, it is three-dimensional with a high Reynolds number. Turbulence manifests through eddies that transfer kinetic energy to smaller eddies in a process known as the energy cascade. This cycle continues until the eddies become so small that the viscous stresses are enough to dissipate the kinetic energy into internal energy. The small scales can also be called Kolmogorov scales. They are much smaller than the characteristic length of the flow and isotropic properties can be assumed even though flow remains a continuum medium [37].

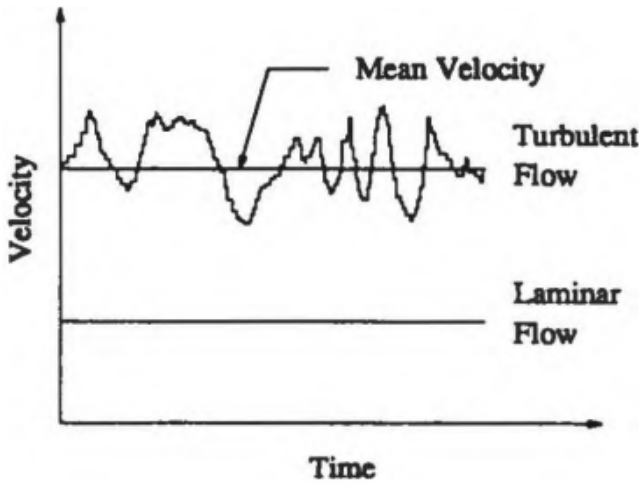

Figure 2.17: Velocity fluctuations for steady laminar and turbulent flow. [35]

With this in mind, to model turbulence in CFD, several numerical methods have been developed to study turbulence and capture its effects.

Reynolds-Averaged Navier-Stokes (RANS)

This approach primarily focuses on examining how turbulent fluctuations affect the average flow. By averaging the Navier-Stokes Equations over time, two components emerge: the mean flow properties and the fluctuating part. This averaging introduces additional terms known as Reynolds stresses, necessitating the use of turbulence models like the k – ε or k – ω models to solve the system. Widely employed in engineering simulations, this method is computationally efficient and generally sufficient for analysing the mean flow properties without delving into turbulent details [38].

Thus, in RANS and other governing flow equations, the values of some properties are replaced by their average, leaving a term called the Reynolds stress tensor, $\tau_{ij}^R = -\rho\overline{u_i' u_j'}$, with the fluctuations [38].

While Reynolds-averaging simplifies the computation by avoiding the need for instantaneous flow field calculations, it introduces a new variable not present in the Navier-Stokes equations which is the Reynolds stress tensor. It represents an additional stress induced by turbulent motions and stems from decomposing the convective term via Reynolds decomposition. As the objective is to remove reliance on instantaneous flow fields in these simplified equations, modeling this term based on the mean flow becomes a necessary challenge [39] [40].

One approach to calculate the Reynolds Stresses in RANS equations involves the Boussinesq approximation. This method assumes a linear correlation between turbulent Reynolds stresses and the mean rate of strain tensor, and it is represented in Equation 2.29 [39] [40].

$$\tau_{ij}^{R} = -\rho\overline{u_i' u_j'} = \mu_t \left(\frac{\partial u_i}{\partial x_j} + \frac{\partial u_j}{\partial x_i} \right) - \frac{2}{3} \left(\rho k + \mu_t \frac{\partial u_k}{\partial x_k} \right) \delta_{ij} \tag{2.29}$$

The only unknown in this equation is the turbulent viscosity, μ_t, which must be determined by the turbulence model. There are many of them available and some of them will be addressed later.

Despite ongoing efforts, a universally applicable RANS turbulence model remains elusive due to the varied behaviour of eddies. For this reason, selecting an appropriate turbulence model depends on the specific application because of the different behaviour between larger and smaller eddies, so when a single turbulence model is used to describe the collective behaviour of all eddies, it fails [40].

Large Eddy Simulation (LES)

An alternative approach to time-averaging is spatial filtering, a fundamental concept in large eddy simulation (LES). In LES, larger eddies are separated from smaller ones through spatial filtering. Initially, eddies above a certain size threshold are identified and subjected to this filtering operation. The filtered flow equations, incorporating both the mean flow and the larger eddies, are then solved over time, typically using methods like the finite volume approach. The influence of the smallest eddies is accounted for through a sub-grid scale RANS model. While this method offers a way to tackle complex geometry in CFD, it demands significant computational resources due to solving the unsteady Navier-Stokes equations. Nonetheless, LES has garnered attention for its ability to handle intricate CFD problems [41] [42].

Direct Numerical Simulation (DNS)

These simulations tackle both the mean flow and all accompanying eddies. Achieving this requires solving the Navier-Stokes equations over time on meshes fine enough to resolve Kolmogorov length scales, where energy dissipation occurs fully. Additionally, the time step must be sufficiently small to capture rapid fluctuations accurately. Due to these stringent computational demands, simulations of this nature are highly resource-intensive, making them impractical for routine engineering CFD applications [43].

Turbulence Models

Amongst the most common turbulence models are the:

Prandtl's mixing length model - This is the most basic model because it operates without introducing any extra transport equations. Instead, it employs an algebraic expression to

depict turbulent Reynolds stress, which varies according to the turbulent flow's location. Although computationally efficient and effective for thin shear layers like jets and wakes, this model falls short in forecasting flow separation and recirculation [44].

Spalart-Allmaras model - This model adds just one transport equation, focusing on turbulent viscosity. It is tailored specifically for aerospace contexts, particularly wall-bounded flows, where it yields precise outcomes even under adverse pressure gradients. However, its accuracy diminishes in certain free shear flows, particularly plane and round jet flows, where it tends to exhibit larger errors [45].

$k - \varepsilon$ model - This model adds two equations, one to model the turbulence kinetic energy, k, and another to model the turbulence dissipation rate, ε. The model demonstrates relatively accurate performance in predicting high Reynolds number flows characterized by near-homogeneous turbulence behaviour with a balance between production and dissipation. However, its efficacy diminishes notably when dealing with boundary layers experiencing adverse pressure gradients [46].
Additionally, it struggles to forecast the viscous sublayer. To address this limitation, suggestions propose incorporating corrections to emulate the law of the wall for incompressible flat-plate boundary layers. For low Reynolds number flows, where turbulent kinetic energy production and dissipation rates may deviate from equilibrium, ad-hoc adjustments of empirical parameters become necessary. Moreover, the standard $k - \varepsilon$ turbulence model exhibits poor performance in shear layers and jets, where turbulent kinetic energy is not balanced with dissipation rates. Lastly, it is advised against employing this model for high swirling/curvature flows, diverging passage flows, and flows influenced by a rotating reference frame [46].

RNG $k - \varepsilon$ model - This model derives from the standard model by adding a statistical technique called renormalization group theory (RNG). It offers enhanced accuracy and reliability across a broader spectrum of flows compared to its standard counterpart. Key enhancements include the introduction of an additional term in the turbulence dissipation rate equation, which improves accuracy, particularly in rapidly strained flows. Furthermore, the model considers swirl effects, eliminating the need for user-specified and constant turbulent Prandtl numbers, instead providing an analytical formula for them through statistical techniques. Additionally, it furnishes an analytically derived differential formula for effective viscosity, facilitating the simulation of low-Reynolds number flows [47].

Realizable $k - \varepsilon$ model - This model represents a newer approach that adheres to mathematical constraints linked to Reynolds stresses, resulting in better alignment with observed turbulent flow phenomena. Neither the standard k- ε model nor the RNG k- ε model is realizable. This model achieves improved accuracy by utilizing an alternative modulation technique for turbulent viscosity and dissipation rate. Specifically, the dissipation rate is derived from a precise equation governing the transport of mean-square vorticity fluctuations. This model predicts more accurately the spreading rate of both planar and round jets. It is also likely to provide superior performance for flows involving rotation, and boundary layers un-

der strong adverse pressure gradients, separation, and recirculation [48].

$k-\omega$ model - This model also adds two equations, one to model the turbulence kinetic energy, k, and another to model the specific dissipation rate, ω which is the ratio of ε to k. This model suits low-Reynolds numbers, compressibility, shear flow spreading and has an advantage over the $k-\varepsilon$ turbulence model because it does not require any wall functions for the calculation of the velocity distribution near walls. As a result, it has better performance for flows with adverse pressure gradient when compared to the other. However, this model exhibits a strong sensitivity to the freestream boundary condition for external flow applications [49].

Shear Stress Transport (SST) $k-\omega$ model - Menter developed this model to combine the strengths of the $k-\omega$ model's accuracy near walls with the free-stream adaptability of the $k-\varepsilon$ model. It converts the $k-\varepsilon$ formulation into a $k-\omega$ framework, aiming for a robust and versatile turbulence model. It is similar to the $k-\omega$ model, but shows improvements, such as both the standard k-ω model and the transformed k-ε model are scaled by a blending function, effectively combining them. This function is designed to activate the k-ω model near walls (where it performs well) and the k-ε model away from surfaces. Also, a damped cross-diffusion term is introduced in the ω equation, enhancing its performance, the definition of turbulent viscosity is adjusted to better capture turbulent shear stress transport, and the different modeling constants are utilized to improve accuracy [50].

2.6.3 CFD Process

In order to perform a CFD analysis it is preferred to follow a sequence of steps that are called the CFD process. These steps include [51]:

1. Formulate the Flow Problem

   It is essential to define the flow problem by addressing key questions about the goal of the analysis, the geometry, and spatial dimensions, the characteristics of the flow, among other important things.

2. Model the Geometry and Flow Domain

   Modeling the body for flow analysis typically involves using CAD software to represent its geometry, which may require simplifications for a manageable analysis. Decisions are made regarding the extent of the flow domain, with some boundaries coinciding with the body's surfaces and others serving as free boundaries for flow entry or exit. This modeling approach considers both the body's geometry and the flow domain to facilitate grid generation, ensuring compatibility between the two aspects during the modeling process.

3. Establish the Boundary and Initial Conditions

Finite flow domain is defined, requiring appropriate boundary conditions. The simulation begins with an initial solution and progresses iteratively until a final flow field solution is achieved.

4. Generate the Grid

   Grid generation is a crucial aspect, involving the discretization of the flow domain into structured grids. These grids must adhere to certain quality criteria, such as orthogonality, relative grid spacing, and skewness, with considerations for boundary layer resolution and turbulence modeling.

5. Establish the Simulation Strategy

   Determining simulation strategy includes taking into account the computational resources, and the available time with the turbulence/chemistry models, and algorithms to obtain the desired accuracy.

6. Establish the Input Parameters and Files

   It is necessary to prepare the required input parameters aligned with the chosen strategy. Additionally, grid and boundary condition information is typically essential and uploaded in this step. Both the grid and initial flow solution must be generated before running the simulation.

7. Perform the Simulation

   The simulation is performed, and the computer solves the flow. There are various possible options for interactive or batch processing and distributed processing.

8. Monitor the Simulation for Completion

   Once the solution converges, the simulation is considered complete. This can be observed if the residuals are smaller than those defined in the simulation strategy.

9. Post-Process the Simulation to get the Results

   Post-processing involves extracting the desired flow properties from the computed flow field, displaying graphics, streamlines, and vector fields, among other desired values.

10. Make Comparisons of the Results

    It is crucial to compare the obtained results with experimental studies or other computational methods to establish the validity of the simulations.

11. Repeat the Process to Examine Sensitivities

    To understand the possible differences in the accuracy of the results it is important to do more in-depth studies, for example, studies where the initial or boundary conditions, dimensions, models, etc., are changed as this enables a deeper understanding of the simulated phenomena.

12. Document

    Documenting everything where the entire process is explained in detail, including each step followed, and exposing the findings.

Chapter 3

Methodology

This chapter presents the methodology that was followed throughout the simulation. All the justifications leading to the results obtained, and all the tools used will be explained and discussed.

3.1 Introduction

In this work a rotating detonation engine model was created based on other research to perform an operating 3D simulation of this engine. A stoichiometric mixture of hydrogen and air was used and a specific setup configuration was chosen and will be explained in the following sections.

The CFD software used was ANSYS Fluent. This software offers various engineering simulation capabilities across many physics domains essential for the design process. Specifically, Fluent, a module within ANSYS, is tailored for fluid dynamics and chemical reaction simulations, making it ideal for this work.

The computer used to create the case has installed an Intel(R) Xeon(R) Silver 4210 CPU with a 2.19 GHz clock and 96 gigabytes of Random Access Memory (RAM). For running the case it has been used a cluster with 20 cores.

The steps used to perform the simulation in ANSYS Fluent were the following:

1. Formulate the flow problem, understanding the goals and possible complications of the simulation;

2. Design the appropriate geometry of the engine;

3. Generate an accurate mesh;

4. Setting up the physical model, such as the equations of fluid motion;

5. Define the boundary conditions, which means specifying the fluid behaviour and properties at all bounding surfaces of the fluid domain;

6. Obtain the solution and analyse the results;

7. Validate the results and discuss them.

3.2 Geometry Preparation

The model was created using CAD (Computer-Aided Design) software in order to be tested afterward. In this work, the software used to create the engine's model was *DesignModeler* available within ANSYS. Figure 3.1 shows a model of a typical internal structure of a RDE from the AFLR (Air Force Research Laboratory) with annotations related to each component [52]. Figure 3.2 shows a view of the engine's CAD model used to perform the simulation. The geometry model used in the simulation was based and created taking into consideration designs of different engine models used in other investigations [52], [53], [54], [55], [56], and [57].

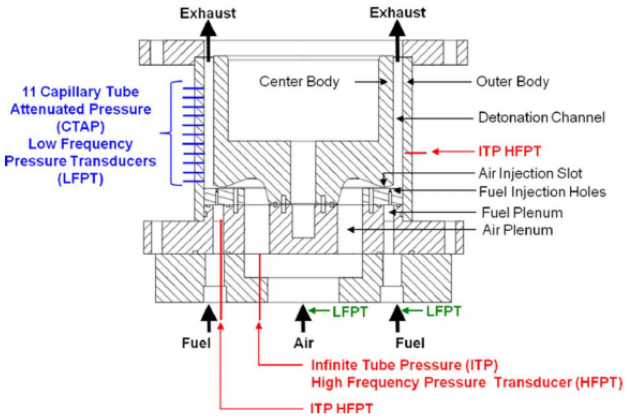

Figure 3.1: Typical internal structure of a RDE from AFRL. [52]

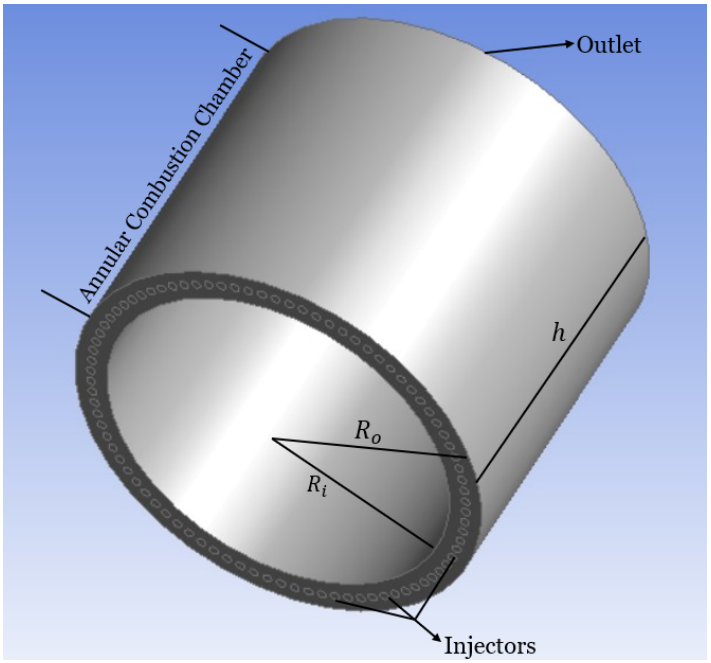

Figure 3.2: Geometry model.

In the simulation, the mixture of hydrogen and air was injected through 86 evenly spaced orifices (injectors) with a radius of 1 mm. The mixture rapidly traveled inside the annular combustion chamber, which has an inner radius (R_i) of 40 mm, an outer radius (R_o) of 47.5 mm, and a height (h) of 80 mm.

These types of simulations, involving combustion but especially detonation, are extremely computationally intensive and require a high level of knowledge on this matter. Therefore, the engine CAD model was simplified to reduce the computational power needed, the time of the simulation itself, and consequently the model complexity.

3.3 Mesh Generation

The next step involved generating a mesh or grid for the 3D model. The primary objective of meshing is to divide the domain into numerous smaller, non-overlapping sub-domains, forming a grid or mesh of cells where the solution will be computed. This phase holds significant importance in a Computational Fluid Dynamics simulation, as the quality of the mesh significantly impacts the accuracy, convergence, and computational efficiency of the solution.

Meshing methods for complex geometries can be categorized into two primary groups, structured grids or unstructured grids. Structured grids are characterized by well-organized elements, typically employing simple shapes like hexahedrons to discretize the flow domain. Conversely, unstructured grids offer advantages for intricate geometries, as they can conform to any shape. These grids typically consist of tetrahedral elements, though they come with certain drawbacks. Tetrahedral elements lack parallel faces, posing challenges in accurately representing flow propagation across them. Consequently, this may result in reduced accuracy, and besides, unstructured grids demand larger memory allocations to store information [58].

Creating the perfect mesh for a specific geometry is a great challenge. A resume of the best practices for meshing is shown in Figure 3.3.

A high-quality mesh meets specific criteria such as orthogonal quality and skewness, ensuring its validity for the intended physics analysis, including boundary layer considerations. It also guarantees grid independence and accurate representation of geometric intricacies. Conversely, a poor-quality mesh can lead to convergence issues, inaccurate depiction of physics phenomena, and diffuse solutions [59].

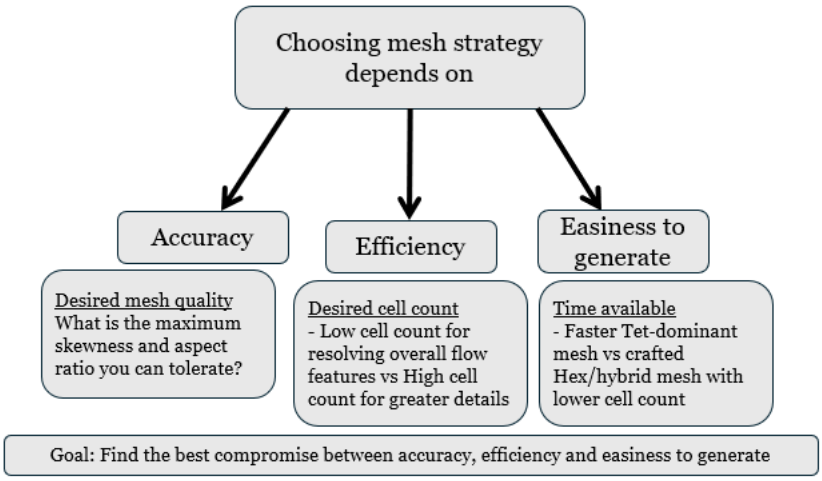

Figure 3.3: Meshing Best Practice Guidelines. [58]

3.3.1 Mesh Quality

Orthogonal Quality

The concept of mesh orthogonality relates to how close the angles between adjacent element faces (or adjacent element edges) are to some optimal angle (depending on the relevant topology) [60]. For a *cell*, computed for each face *i*, is the minimum of:

$$\frac{A_i f_i}{\left|\vec{A_i}\right|\left|\vec{f_i}\right|} \quad , \quad \frac{A_i c_i}{\left|\vec{A_i}\right|\left|\vec{c_i}\right|} \tag{3.1}$$

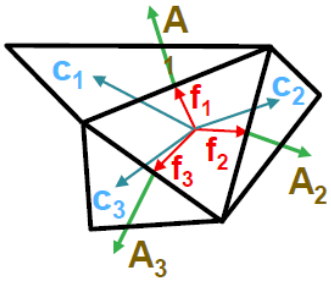

Figure 3.4: Representation of a *cell*. [60]

where A_i is the face normal vector, f_i is a vector from the centroid of the cell to the centroid of that face, and c_i is a vector from the centroid of the cell to the centroid of the adjacent cell.

Skewness

Two methods for determining skewness: Equilateral volume deviation and normalized angle deviation represented by Equations 3.2 (applies only for triangles and tetrahedrons), and 3.3,

respectively [60].

$$Skewness = \frac{optimalcellsize - cellsize}{optimalcellsize} \tag{3.2}$$

$$Skewness = \max\left[\frac{\theta_{max} - \theta_e}{180 - \theta_e}, \frac{\theta_e - \theta_{min}}{\theta_e}\right] \tag{3.3}$$

Where the subscript e stands for the equiangular face/cell (90 degrees for quads and hexas or 60 degrees for tets and tris).

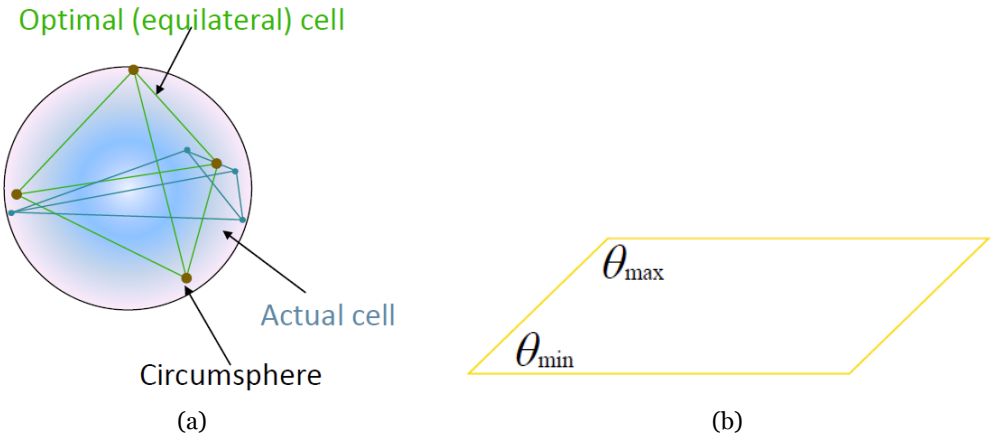

Figure 3.5: (a) Equilateral Volume Deviation; (b) Normalized Angle Deviation. [60]

The mesh generation was performed using ANSYS. Firstly, the option Fluid in the Fluid/Solid area was selected in the Geometry section under the Material subsection. After that, the right configurations in the mesh section are chosen. The full mesh configuration is shown in Table 3.1.

Table 3.1: General Mesh Configurations.

Defaults	
Physics Preference	CFD
Solver Preference	Fluent
Element Order	Linear
Element Size	1 mm
Export Format	Standard
Export Preview Surface	No
Inflation	
Use Automatic Inflation	None
Inflation Option	Smooth Transition

Table 3.1: General Mesh Configurations(continued).

Sizing	
Use Adaptive Sizing	No
Growth Rate	Default (1.2)
Max Size	Default (2 mm)
Mesh Defeaturing	Yes
Defeature Size	Default (5e-3)
Capture Curvature	Yes
Curvature Min Size	Default (1e-2)
Curvature Normal Angle	Default (18 °)
Capture Proximity	No
Quality	
Check Mesh Quality	Yes, Errors
Target Skewness	Default (0.9)
Smoothing	Medium
Advanced	
Number of CPUs for Parallel Part Meshing	Program Controlled
Triangle Surface Mesher	Program Controlled
Topology Checking	Yes
Pinch Tolerance	Default (9e-3)
Generate Pinch on Refresh	No
Statistics	
Nodes	1929706
Elements	1878633

The *MultiZone* mesh method was selected for the entire body. This method provides an automatic decomposition of geometry into mapped structured regions. It automatically generates a pure hexahedral mesh where possible and then fills the more difficult-to-capture regions with unstructured mesh. For the injectors, it was desired to obtain a refined mesh. Therefore, a *face sizing* for the injectors was created to improve the mesh quality. The details of the local sizing can be seen in Table 3.2.

Table 3.2: Face Sizing Configuration.

Scope	
Scoping Method	Geometry Selection
Geometry	86 Bodies
Definition	
Suppressed	No
Type	Element Size
Element Size	0.2 mm
Advanced	
Defeature Size	Default (5e-3 mm)
Influence Volume	No
Behaviour	Hard
Capture Curvature	No
Capture Proximity	No

The final mesh is shown in Figure 3.6, a detailed view of the injectors' mesh is in Figure 3.7, and the mesh metrics graphics of the Orthogonal Quality, and the Skewness are represented in Figures 3.8,

and 3.9, respectively. In these Graphics, the different element types are plotted with different color bars and they can be used to help locate poor quality elements, in this case only one type of element was obtained.

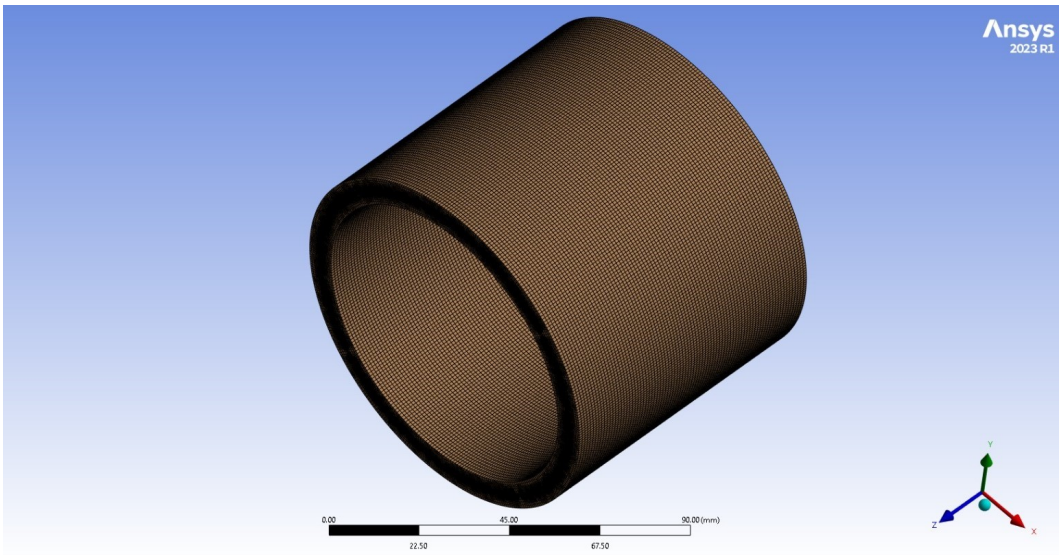

Figure 3.6: Mesh.

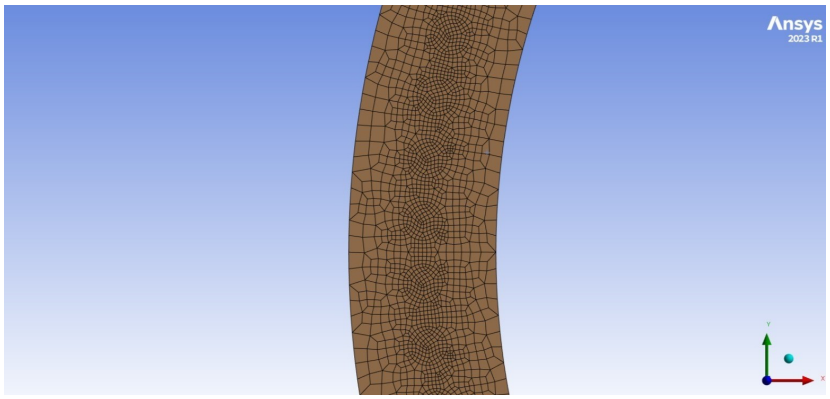

Figure 3.7: Detailed mesh view of the injectors in the XY plane.

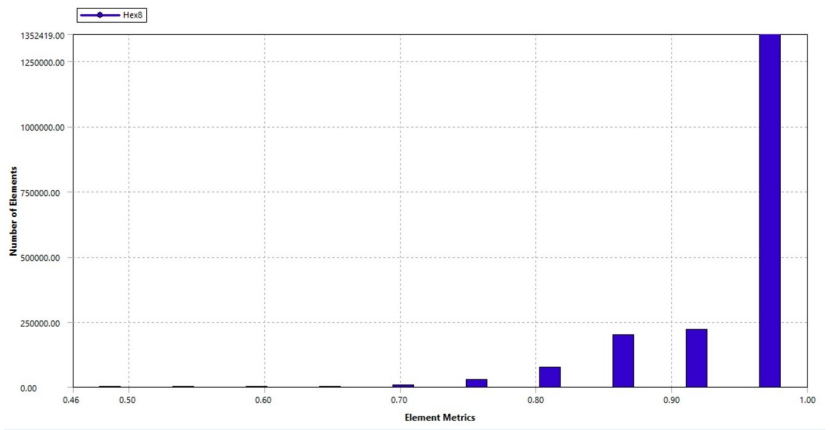

Figure 3.8: Orthogonal Quality.

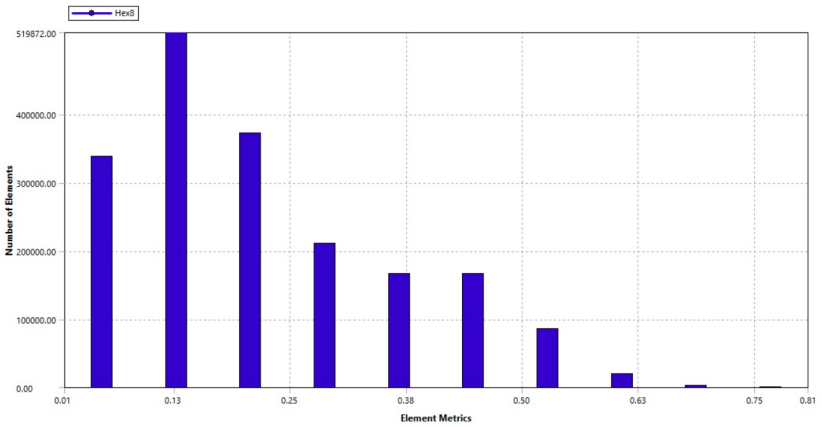

Figure 3.9: Skewness.

3.4 Physics set up

Once the mesh is ready, the problem setup can start. As mentioned before, ANSYS Fluent was the software used to conduct the simulations.

When initiating ANSYS Fluent, a Fluent Launcher window will appear, where several settings for the simulation must be chosen. Firstly, the 3D dimension option was selected. Secondly, to improve accuracy, double precision was also chosen, though this will slow down the computation slightly. To optimize performance, parallel processing and the number of processes were selected, 19 was the number chosen because it was almost the maximum available on the computer. Using parallel processing will significantly reduce the computational time.

Once Fluent is launched, it is essential to verify the quality of the mesh, which can be done by ”report the quality” in the General-setup Mesh box. Among the available mesh quality parameters, orthogonal quality, and mesh skewness are of great importance. Tables 3.3 and 3.4 serve as guides in their evaluation, respectively.

Table 3.3: Orthogonal quality mesh metrics spectrum. [59]

Unacceptable	Bad	Acceptable	Good	Very Good	Excellent
0-0.001	0.001-0.14	0.15-0.20	0.20-0.69	0.70-0.95	0.95-1.00

Table 3.4: Skewness mesh metrics spectrum. [59]

Excellent	Very Good	Good	Acceptable	Bad	Unacceptable
0-0.25	0.25-0.50	0.50-0.80	0.80-0.94	0.94-0.97	0.98-1.00

Generally, to have a good-quality mesh is desired to keep the minimum orthogonal quality above 0.15, and the maximum skewness below 0.94. The model presented a minimum value of orthogonal quality of 0.45865 and an average of 0.9507. In terms of skewness, it presented a maximum value of 0.8075 and an average of 0.21998. Therefore, the mesh is of good quality.

3.4.1 Models

Besides continuity and momentum equations, a variety of additional models can be selected or activated for a given simulation in Fluent. These models can be chosen depending on the necessity of the simulation. In this work, the following models were used [61]:

- Energy model - The energy model must be activated as this regards the energy related to the temperature change within the combustion process or heat transfer.
- Viscous model - Through this model, laminar and turbulent flows can be studied. The chosen model was the Realizable $k-\varepsilon$ mainly because this model demonstrates superior performance, particularly in flows characterized by strong streamline curvature, vortices, and rotation. More information about the potentialities of this model was discussed in subsection 2.6.2.
- Species model - This model allows ANSYS Fluent to model the mixing, transport, and combustion of chemical species. Due to the importance of this model for this work, the inputs will be explained in detail in the next sub subsection 3.4.1.1.

3.4.1.1 Species model

The species model was chosen taking into consideration the three options available in Fluent for premixed combustion. The options were species transport, premixed combustion, and composition PDF (Probability Density Function) transport. The chosen one was species transport because it is suitable for a wide range of applications including laminar or turbulent reaction systems and combustion systems with premixed, non-premixed, or partially-premixed systems.

It models the mixing and transport of chemical species by solving conservation equations describing convection, diffusion, and reaction sources for each component species. Additionally, due to the already demanding computational power, the species transport model presents a good balance between accuracy and computational power, being the best choice for this work.

In the "species model" panel, the volumetric reaction box was enabled after selecting the species transport model. Also, from the additional options available, the diffusion energy source that adds the enthalpy transport effect in the energy equation was selected. When the species transport model is selected, the software predicts the mass fraction of each input species by solving the conservation equation for each inputted chemical species. To do that the reaction rates that appear as source terms can be computed by one of these turbulence-chemistry interaction models:

- Laminar Finite-Rate model: Computes chemical reaction rates based on the assumption of laminar (non-turbulent) flow. It relies on detailed reaction mechanisms and considers the actual finite rate of chemical reactions without assuming any turbulent mixing effects;
- Finite-Rate/ Eddy-Dissipation: Combines detailed chemical kinetics with turbulent mixing effects. It considers both the finite rate of chemical reactions and the turbulent mixing, where the overall reaction rate is controlled by the slower of the two processes;
- Eddy-Dissipation: Reaction rates are assumed to be controlled by turbulence, so Arrhenius chemical kinetic calculations are avoided. The model is computationally cheap, but for realistic results only one or two-step heat-release mechanisms should be used;

- Eddy-Dissipation Concept: Extends the Eddy-Dissipation model by incorporating detailed chemical kinetics within small turbulent structures known as fine structures. It allows for the detailed reaction mechanisms to be resolved within these small-scale turbulent regions but at a high computational cost.

The laminar finite-rate chemistry model was employed to solve for the reacting flow in the combustion chamber, thereby not accounting for turbulence-chemistry interaction. This choice was validated through two other investigations [52] [54] that used the same model.

The next step in the species model was specifying the mixture material and defining the properties of the mixture. The mixture material may be thought of as a set of species and a list of rules governing their interaction. Mixture properties include the species in the mixture, the reaction, and other physical properties, such as viscosity or specific heat.

For specifying the mixture, the Fluent database was used, since it had hydrogen-air mixture available. Some properties of the mixture were changed to make the mixture as close to real conditions as possible. Table 3.5 shows the mixture properties.

Table 3.5: Mixture Properties - options.

Mixture Species	names
Reaction	finite-rate
Mechanism	reaction-mechs
Density (kg/m^3)	ideal gas
C_p (J/kgK)	mixing-law
Thermal Conductivity	mass-weighted-mixing-law
Viscosity (kg/ms)	mass-weighted-mixing-law
Mass Diffusivity (m^2/s)	kinetic-theory
Laminar flame speed (m/s)	constant, 0.2

3.4.2 Boundary Conditions

One of the most important steps of this entire work is correctly defining the boundary conditions as this greatly affects convergence and results. Thus, all of the input values for the boundary conditions are explained in this section. Three types of boundary conditions were applied: walls, pressure outlet, and pressure inlet.

The wall boundaries have remained at default settings (stationary wall and no-slip condition) with a temperature of 300 K in the thermal conditions tab, and in the species boundary conditions tab, a zero diffusive flux for all species was selected.

The boundary conditions for the inlet and the outlet are shown in Tables 3.6, and 3.7, respectively.

For calculating the supersonic initial pressure, a UDF (User-Defined Function) was created. This function is also going to control the injection phase. It will analyse the current pressure inside the chamber and determine if the injectors will inject more mixture or not. It does this by reading the pressure inside the chamber, if that pressure is superior to the stagnation pressure of the inlet the flow is at stagnation (Mach = 0) and the supersonic initial pressure is equal to the stagnation pressure. If the pressure is intermediate between the critic pressure and the stagnation pressure, meaning Mach below 1, the injection is subsonic and the supersonic initial pressure is equal to the chamber pressure.

Table 3.6: Inlet Boundary Conditions.

Pressure Inlet		
Momentum	Reference Frame	Absolute
	Gauge Total Pressure	1013250 Pa
	Supersonic/Initial Gauge Pressure	UDF - Pressure Inlet
	Direction Specification Method	Normal to Boundary
	Specification Method	Intensity and Viscosity Ratio
	Turbulent Intensity	2 %
	Turbulent Viscosity Ratio	5
Thermal	Total Temperature	300 K
Species - Species Mass Fraction	H_2	0.029
	O_2	0.230

Table 3.7: Outlet Boundary Conditions.

Pressure Outlet		
Momentum	Backflow Reference Frame	Absolute
	Gauge Pressure	101325 Pa
	Backflow Direction Specification Method	Normal to Boundary
	Specification Method	Intensity and Viscosity Ratio
	Backflow Turbulent Intensity	2 %
	Backflow Turbulent Viscosity Ratio	5
Thermal	Backflow Total Temperature	300 K

If the pressure is inferior or equal to the critic pressure, the supersonic initial pressure will be equal to the critic pressure and injection will be happening having Mach = 1.

To apply this function, the following procedure was made in Fluent: In Define > User-Defined > Functions > Compiled, in the source files the UDF file was added and the library was built and then loaded. Appendix A shows the used code.

3.5 Solution

This section discusses the main tasks related to solving the numerical calculations required to achieve a valid and correct solution for the simulation. Until here, the setup for the flow simulation was prepared. To obtain a solution, we can modify the solver settings improving both the rate of convergence and the accuracy of the results.

The fluxogram in Figure 3.10 shows the basic workflow of the solution procedure for a simulation [62].

3.5.1 Choosing a Solver

There are two kinds of solvers available in ANSYS Fluent:

- Pressure-based
- Density-based

Figure 3.11 shows a scheme of the available solvers and some of their characteristics.

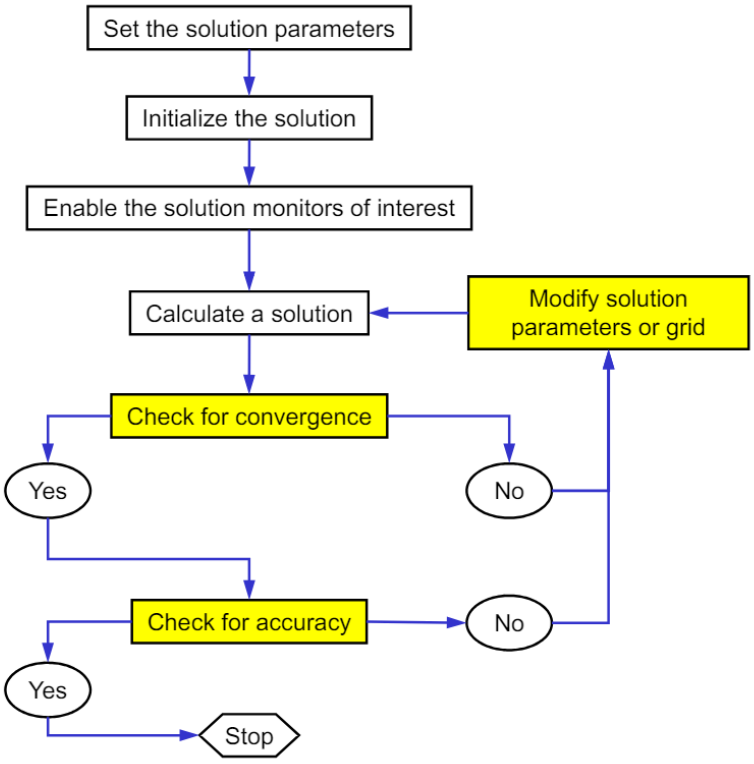

Figure 3.10: Solution Procedure Workflow. [62]

The pressure-based solver is versatile, handling a wide range of flow regimes from low-speed incompressible flows to high-speed compressible flows. It requires less memory for storage and offers flexibility in how the solution procedure is implemented. The pressure-based coupled solver (PBCS) is suitable for most single-phase flows and offers better performance compared to the standard pressure-based solver. However, it's not available for multiphase (Eulerian), periodic mass-flow, and non-iterative time advancement (NITA) cases. This solver also requires 1.5 to 2 times more memory than the segregated solver [62].

The density-based coupled solver (DBCS) is best used when there's a strong interdependence between density, energy, momentum, and species, making it ideal for specific complex flow scenarios, such as high-speed compressible flows with combustion, hypersonic flows, and flows with significant shock interactions. In this solver, equations for continuity, momentum, energy, and species (if required) are solved in vector form. Pressure is obtained through an equation of state and additional scalar equations are solved in a segregated way. [62]

Due to the nature of this study, the density-based solver was used because it is mainly used for high-speed compressible flows, especially flows with shock interactions. However, this solver typically makes the simulation longer, it becomes a necessary trade-off to have convergence. [63]

3.5.2 Formulation, Flux Type, and Discretisation

The DBCS can be run either explicit or implicit. Implicit uses a point-implicit GaussSeidel / symmetric block Gauss-Seidel / ILU method to solve for variables. Explicit uses a multi-step Runge-Kutta explicit time integration method. The explicit formulation was chosen sustained in two articles [54] [57].

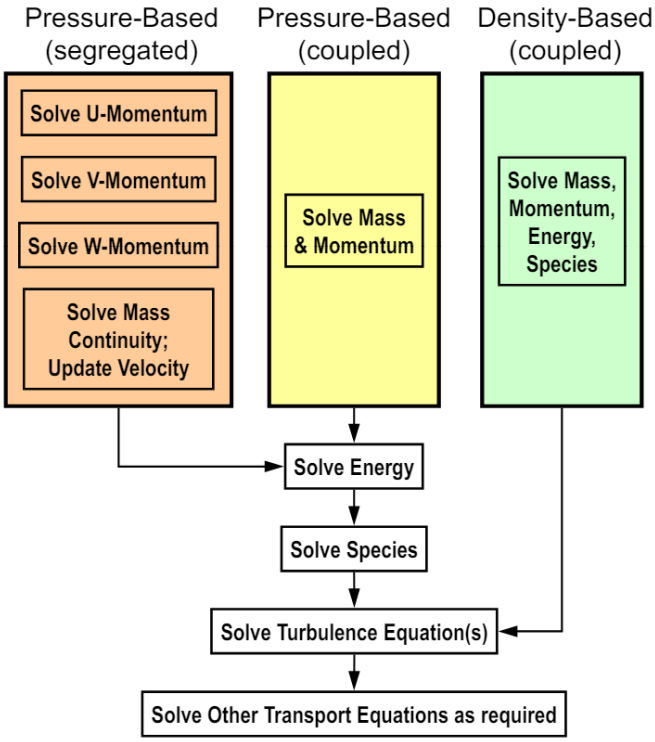

Figure 3.11: Solver Settings. [62]

In Fluent, solver variables are stored at the center of grid cells (control volumes). To solve the equations, field variables at cell centers must be interpolated to the faces of the control volumes.

The interpolation schemes for the convection term include [62]:

- First-Order Upwind: Easiest to converge, but only first-order accurate;
- Second-Order Upwind: Utilizes larger stencils for second-order accuracy, essential for triangular/tetrahedral meshes or when the flow is not aligned with the grid. However, convergence may be slower;
- Monotone Upstream-Centered Schemes for Conservation Laws (MUSCL): A locally third-order convection discretization scheme for unstructured meshes, more accurate for predicting secondary flows, vortices, forces, etc;
- Quadratic Upwind Interpolation (QUICK): Applicable to quadrilateral/hexahedral and hybrid meshes, useful for rotating or swirling flows, and third-order accurate on a uniform mesh.

Gradients of solution variables are needed to evaluate diffusive fluxes, velocity derivatives, and for higher-order discretization schemes. These gradients at cell centers can be determined using three methods [62]:

- Green-Gauss Cell-Based: The least computationally intensive method, but the solution may exhibit false diffusion;
- Green-Gauss Node-Based: More accurate and computationally intensive, minimizes false diffusion, recommended for unstructured meshes;

- Least-Squares Cell-Based: The default method, offers the same accuracy and properties as the node-based gradients but with less computational intensity.

For gradient calculations, the Least-Squares Cell-Based method was employed. The Second Order Upwind scheme was chosen for the flow as it offers significant advantages in handling complex flows. For turbulent kinetic energy and turbulent dissipation rate, the first-order scheme was used to ensure stability and reliable results and to save some computational power.

For the flux type, there are two options available Roe-FDS (Roe flux-difference splitting) and AUSM (Advection Upstream Splitting Method). The first one splits the fluxes in a manner that is consistent with their corresponding flux method eigenvalues. The second one provides exact resolution of contact and shock discontinuities and it is less susceptible to Carbuncle phenomena (numerical instability that affects the numerical capturing of shock waves when low-dissipative upwind scheme is used). The AUSM was chosen.

It is also necessary to specify the desired transient formulation. The second-order implicit formulation is accurate enough and was the selected option. Table 3.8 shows the options chosen.

Table 3.8: Solution Methods.

Formulation	Explicit
Flux Type	AUSM
Gradient	Least Squares Cell Based
Flow	Second Order Upwind
Turbulent Kinetic Energy	First Order Upwind
Turbulent Dissipation Rate	First Order Upwind
Transient Formulation	Second Order Implicit

3.5.3 Initialization

The solver works iteratively. Therefore before the very first iteration, a value must exist for every quantity in every grid cell. The more realistic the value, the better (quicker) convergence will be. First, the hybrid initialization was done and then the standard initialization computed from the outlet was done. After the standard initialization, it was necessary to create two *Patch* regions. The first region was filled with fresh mixture and the second region was the ignition zone and was created inside the first region. This zone was much thinner and had high pressure, temperature, and velocity. This ignition method was also used in [64]. From this point, the detonation occurred and the detonation cycle began. Both regions are in Figures 3.12(a), and 3.12(b), respectively.

3.5.4 Convergence

The solver should be given sufficient iterations to converge the problem. At convergence, the following should be satisfied: The solution no longer changes with subsequent iterations, overall mass, momentum, energy, and scalar balances are achieved, and all equations (momentum, energy, etc.) are obeyed in all cells to a specified tolerance.

The convergence criteria chosen are in Table 3.9.

Another crucial metric for determining model convergence is the overall heat and mass balance. The net flux imbalance, displayed as Net Results, should be less than 1% of the smallest flux through the

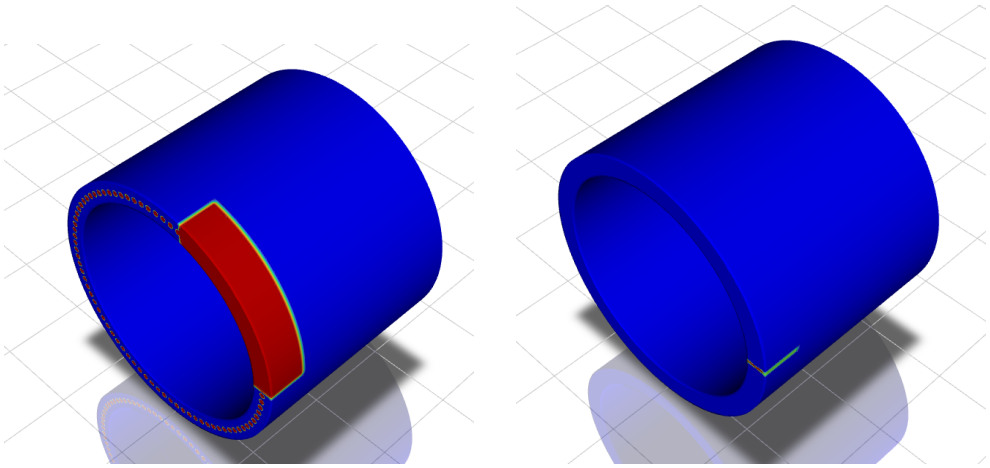

(a) (b)

Figure 3.12: (a) Region 1; (b) Region 2.

Table 3.9: Convergence Criteria.

Residual	Absolute Criteria
continuity	1e-3
x-velocity	1e-3
y-velocity	1e-3
z-velocity	1e-3
energy	1e-6
k	1e-3
epsilon	1e-3
H_2	1e-3
O_2	1e-3
H_2O	1e-3

domain boundary, and if solution monitors suggest convergence but the solution continues to change or exhibits a significant mass/heat imbalance, it indicates that the solution is not yet fully converged.

3.5.5 Under-Relaxation Factors

It's recommended to start with the default under-relaxation factors. If the factor is set too high, the model may become unstable and fail to converge. Conversely, if the factor is set too low, convergence will take longer, requiring more iterations. The default settings are generally appropriate for a wide range of problems, but they can be reduced if necessary. The best settings are often determined through experience. The Under-Relaxation Factors used are shown in Table 3.10.

Table 3.10: Under Relaxation Factors.

Turbulent Kinetic Energy	0.4
Turbulent Dissipation Rate	0.8
Turbulent Viscosity	0.4
Reactions	1
Solid	1

3.5.6 Calculation Activities, and Reports

In order to later see and analyse what is happening inside the combustion chamber, in the *Calculation Activities* panel, an *Autosave* task for every 50 time steps was created to be performed during the

simulation, and in the *Solution* panel, reports of important data were set up. To finish the setup, in the *run calculation* panel, the number of time steps was chosen (12000) as well as the time step size (1e-7 s), and the maximum number of iterations per time step (50). The data sampling was also enabled to keep track of the simulation time. With this, the setup is completed.

Chapter 4

Results

Throughout this study, numerous simulations were conducted, although many were incomplete due to various challenges, ranging from cluster errors to Fluent software bugs or problems with convergence. The most significant hurdle was identifying an effective and appropriate combination of the models with all the required details and specifications for obtaining an accurate solution at a relatively low computational cost. Initially, several attempts were made, each requiring extensive computational time. Consequently, the final results represent the culmination of many months of rigorous simulations and iterative refinements.

In this Chapter, the results of the simulation will be described sequentially, beginning with the analysis of the detonation start and continuing until the last important details of the studied simulation, explaining all the phenomena and details that happened in between. Results of one simulation where a mixture of hydrogen and oxygen instead of hydrogen and air was used will also be presented and compared against the other results.

4.1 Initial Detonation

In the first time steps of the simulation, detonation started and an initial detonation wave appeared. It was formed due to the patch that was created to simulate the ignition. This wave travels inside the annular combustion chamber until deflagration starts to happen because of the fresh mixture that was not burned. The formation of the initial detonation wave can be seen through the contours of pressure and temperature in Figures 4.1 and 4.2, respectively, after 22 microseconds of simulation time. Figures 4.3 and 4.4 also show the contours of pressure and temperature but the fuel used was a mixture of hydrogen and oxygen instead of hydrogen and air, after 25.7 microseconds of simulation time.

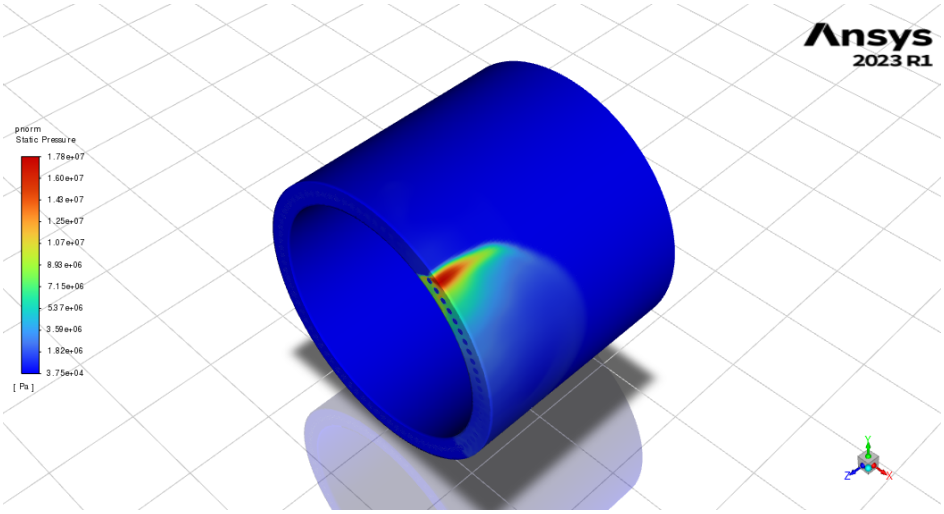

Figure 4.1: Contours of Pressure using Hydrogen-Air.

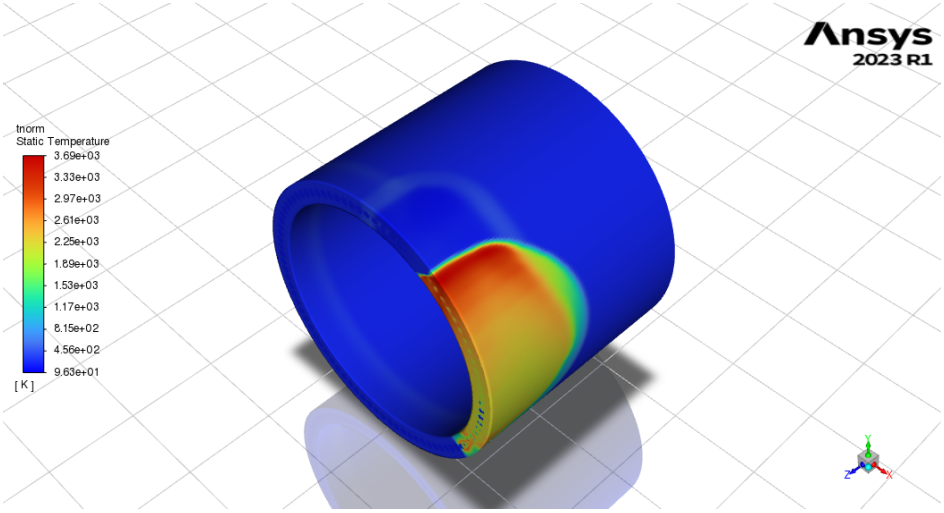

Figure 4.2: Contours of Temperature using Hydrogen-Air.

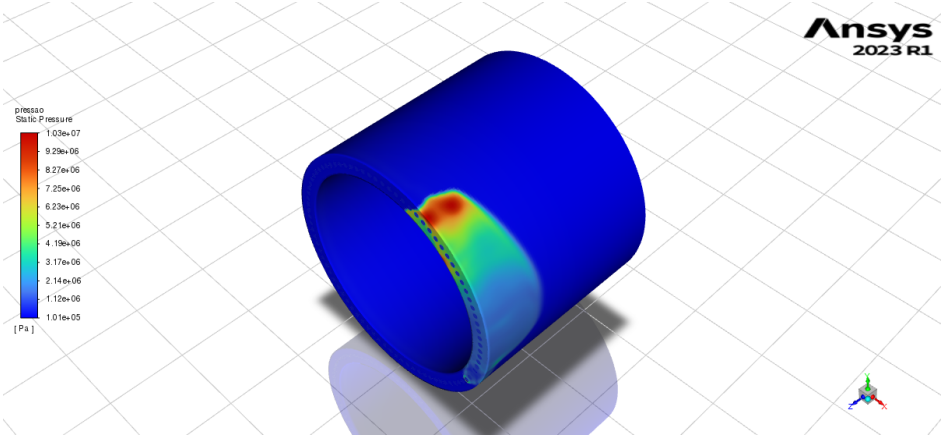

Figure 4.3: Contours of Pressure using Hydrogen-Oxygen.

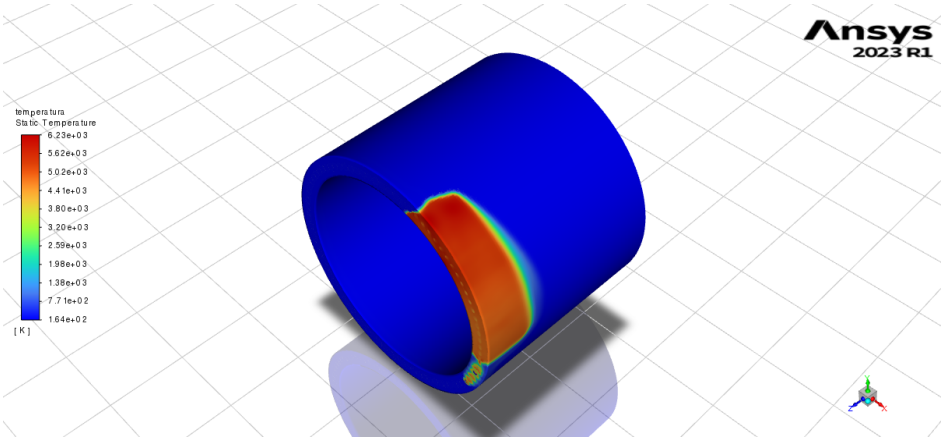

Figure 4.4: Contours of Temperature using Hydrogen-Oxygen.

After ignition, this initial wave travels at supersonic speeds around the annular chamber. The detonation wave is a high-pressure, high-temperature front that compresses and ignites the fuel-air mixture as it travels through the chamber. Deflagration happens a few time steps later due to the presence of mixture that was not burned before. In an ideal RDE this deflagration does not happen or it's almost

insignificant, and the detonation wave continues propagating around the annular chamber, moving continuously in a circumferential direction. Even with many numerical simplifications, the engine model can capture non-idealities relevant to understanding its operation.

4.2 Counter-Rotating Waves

A few time steps later, two waves appear in counter-rotation. This happens due to the mechanism of the detonation initiation and it is something that with the chosen initiation mechanism it is not possible to avoid because the combustion chamber is filled with fuel, making the combustion propagate in two directions once ignition is carried out. At this time, local hot spots will even generate reverse detonation waves, which will collide and evolve in the process of propagation. The formation of this phenomenon can be seen in Figures 4.5 and 4.6 where 74 microseconds and 83.2 microseconds of simulation time have passed, respectively.

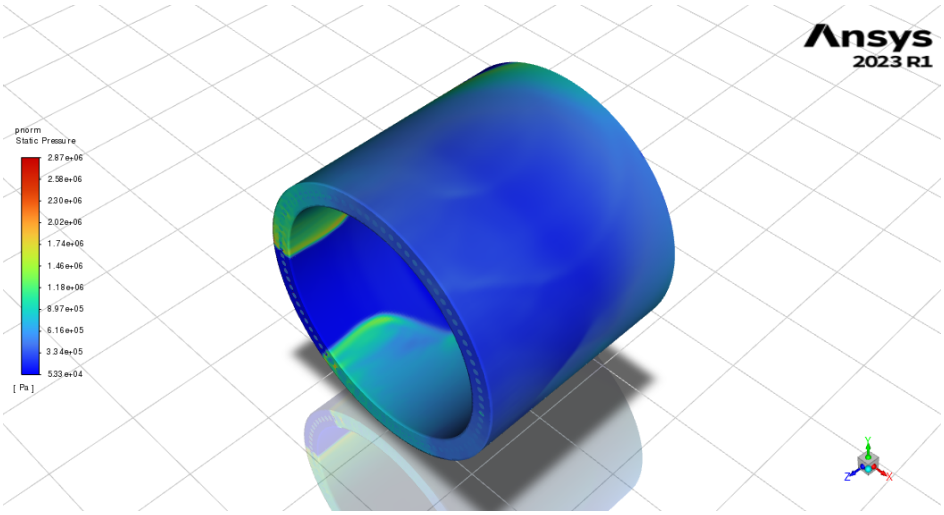

Figure 4.5: Contours of Pressure showing the formation of two waves in counter rotation using Hydrogen-Air.

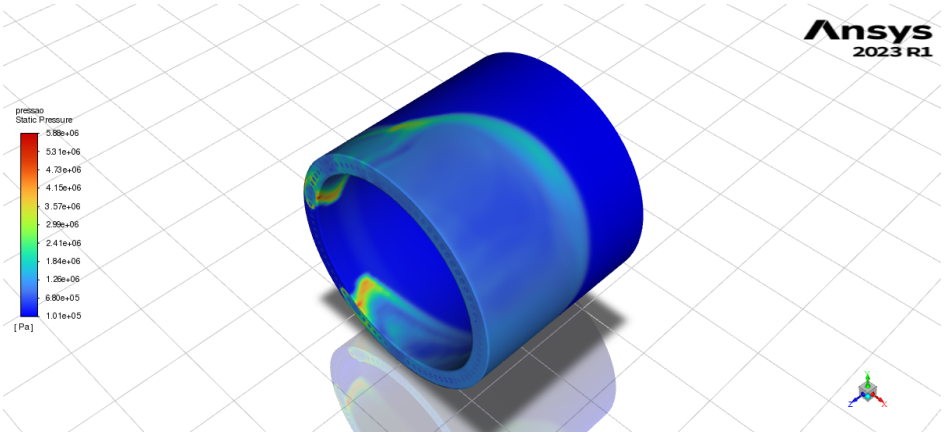

Figure 4.6: Contours of Pressure showing the formation of two waves in counter rotation using Hydrogen-Oxygen.

At this point, both simulations are behaving similarly and a second wave appears travelling in an opposite direction in both simulations, it forms because it finds fresh mixture and immediately burns. However, in Figure 4.5 the maximum pressure is 2.87 MPa and in Figure 4.6 is 5.88 MPa, almost two times greater. Also, when using a mixture of hydrogen and air, the waves' fronts are straighter and taller than those in Figure 4.6.

This has an impact on the efficiency of the engine and it is something that is being studied to understand how it can be avoided [65]. One solution presented to launch a single detonation wave rotating in only one direction was that the orifices could be opened not simultaneously but in a sequence [66]. This would require a more complex setup and more computational power but it would be interesting to study further and understand if it dissipates the problem.

4.3 Reversed Flow

Another limitation of the study was found at this point. There will always be reversed flow in the inlet. Reversed flow in the inlet has been reported in a significant amount of CFD simulations of RDEs. It is typically caused by high-pressure waves reflecting back into the inlet. This is not ideal because it will reduce the engine efficiency and eventually make the detonation unstable. However, as long as it does not cause catastrophic instability or detonation failure the simulation results are still a valid representation of RDE dynamics [67] [68]. Using advanced inlet designs or optimizing injector placement can reduce this phenomenon although its presence is somehow close to reality and difficult to avoid in a practical case [68].

Moreover, in this simulation it was found that when the pressure inside the combustion chamber was superior than the stagnation pressure in the inlet, backflow occurred and exhaust gases entered back in the inlet. When the pressure inside the chamber went down and the injection started again, the injectors immediately injected fresh mixture not taking into account the other combustion products. Although, some high pressure combustion products that would produce thrust were lost, the effect of reverse flow is small because only a relatively small percentage in each instant is, in fact, in backflow.

4.4 Stable Operation

After the initiation mechanism we want the engine to reach stable operation which means a single detonation wave travelling circumferentially inside the annular combustion chamber. So after a few time steps, one single detonation wave became more and more evident. However, in the simulation with the stoichiometric mixture of hydrogen and oxygen, surprisingly, deflagration happened and the detonation did not prevail. Figures 4.7 and 4.8 show contours of pressure and temperature using the mixture of hydrogen and oxygen where deflagration happened after 90.3 microseconds of simulation time.

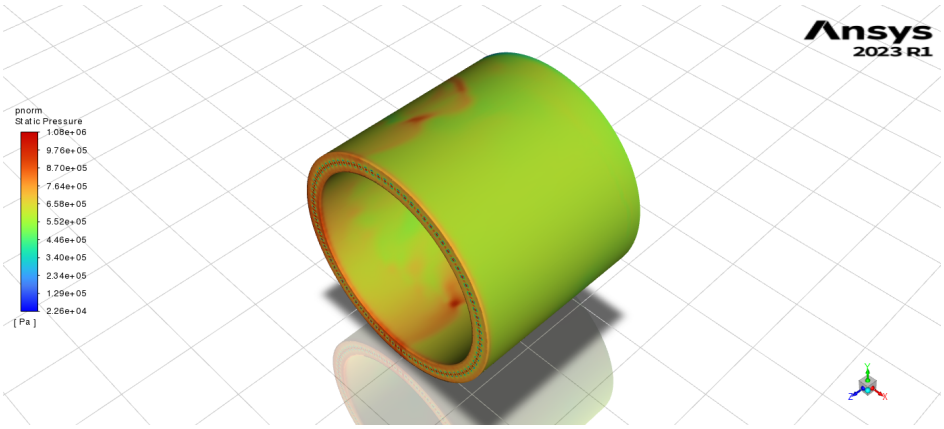

Figure 4.7: Contours of Pressure showing Deflagration.

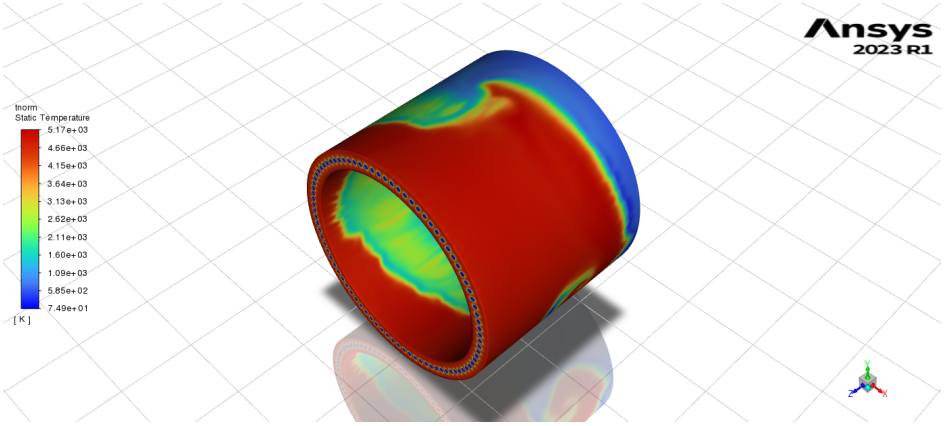

Figure 4.8: Contours of Temperature showing Deflagration.

As we can see in Figure 4.8, the temperature of the annular combustion chamber rose and we can not see the front of the detonation wave. Furthermore, Figures 4.7 and 4.8 show a shock and not detonation as there is no coupled chemistry. A shock refers to a sudden, sharp disturbance that propagates through a medium. It does not involve any accompanying chemical reactions in the medium. A detonation involves a shock wave that is coupled with a chemical reaction (in this case combustion). This coupling means that the energy released from the chemical reaction sustains and propagates the wave at a high speed, much faster than ordinary sound waves.

This might have happened because when pure oxygen instead of air is used, the energy release rate increases due to the higher concentration of oxygen. This can cause instabilities or pre-detonation reactions that could prevent the formation of a stable detonation wave. Instead of transitioning to detonation, the mixture might sustain deflagration (a slower, subsonic flame front) due to these instabilities. Initial conditions of pressure, temperature and velocity also influence how the engine behaves. This phenomenon is an interesting subject to study in future works.

The Chapman-Jouguet (C-J) detonation velocity varies depending on the type of fuel mixture and the conditions under which combustion occurs. This velocity for a stoichiometric mixture of hydrogen and oxygen is higher than for a stoichiometric mixture of hydrogen and air. This happens due to the presence of nitrogen in the air, which does not directly participate in combustion and acts as an inert gas, absorbing some of the released energy. For that reason, due to a higher C-J velocity when using a hydrogen and oxygen mixture, the mesh needed to be more refined and the timestep smaller.

On the other hand, in the simulation with hydrogen and air mixture, this did not happen and a single detonation wave formed and travelled inside the annular combustion chamber. Figure 4.9 shows the contours of temperature after 356 microseconds of simulation time where we can see the detonation wave front and heat columns behind the front of the wave due to the combustion products.

In Figure 4.9 the first detonation wave front is shown, after that, the stable operation of the RDE engine continued. Figure 4.10 shows the detonation wave in its third revolution around the annular combustion chamber. Figures 4.11, 4.12 and 4.13 show a detailed view inside the annular combustion chamber for a better understanding of what is happening inside the chamber in the same time frame as Figure 4.10.

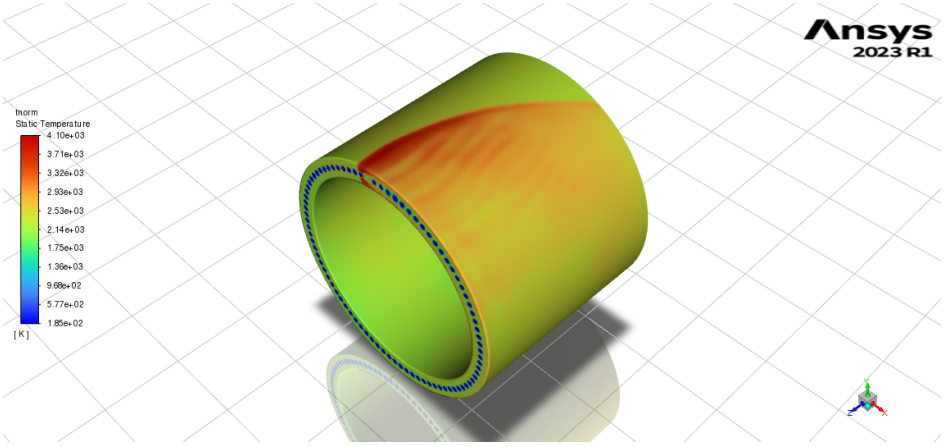

Figure 4.9: Contours of Temperature showing the Detonation Wave (First revolution).

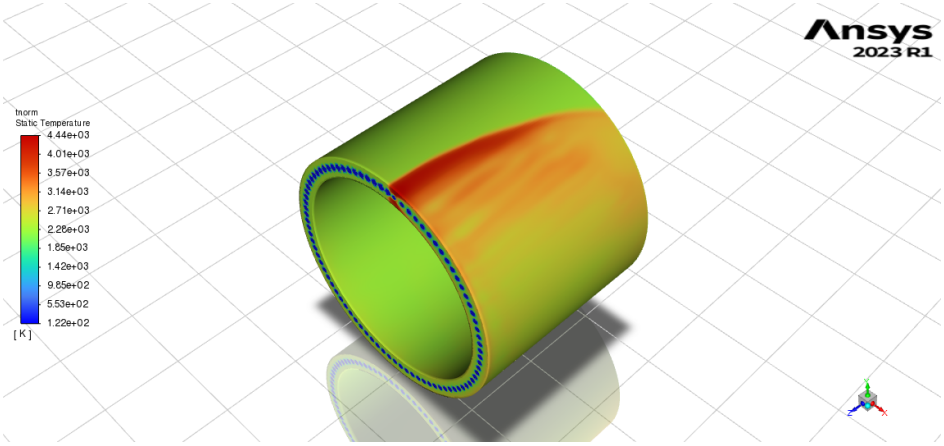

Figure 4.10: Contours of Temperature showing the Detonation Wave (Third revolution).

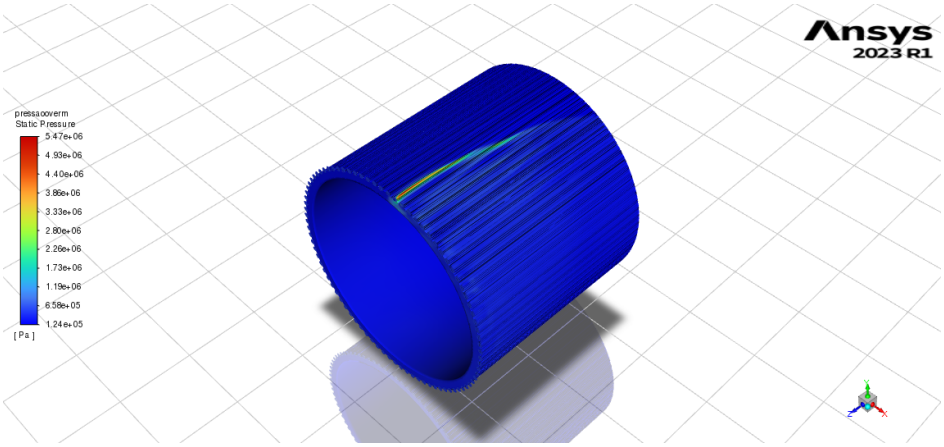

Figure 4.11: Contours of Pressure inside the Combustion Chamber.

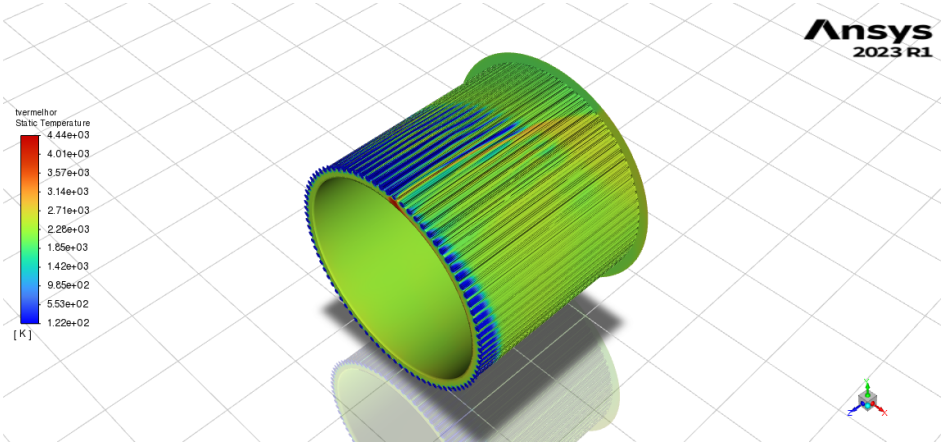

Figure 4.12: Contours of Temperature inside the Combustion Chamber.

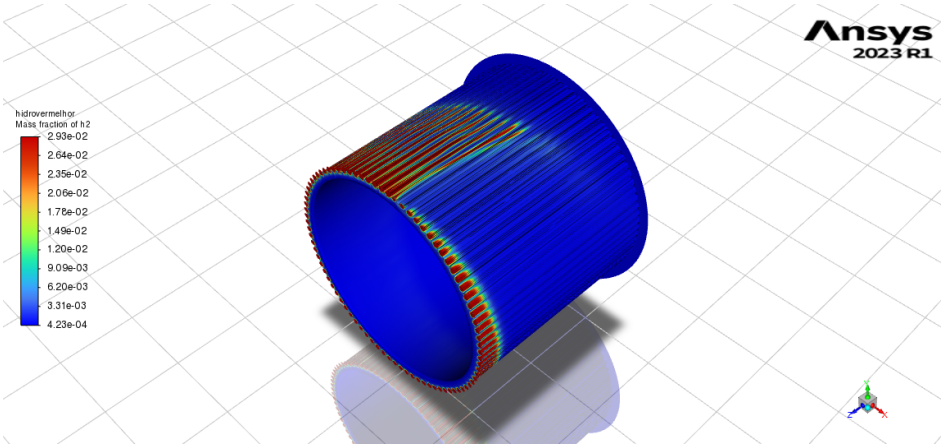

Figure 4.13: Contours of H2 Mass Fraction inside the Combustion Chamber.

In Figure 4.12 we can see fresh mixture in blue near the injectors, combustion products from the current cycle near the hotter red spot and products from the previous cycle in green. The detonation wavefront is moving in the anticlockwise direction and prepares to burn the fresh mixture ahead that can be seen in Figure 4.13 in red.

At each time step during the simulation, data reports with important values of pressure, temperature and other properties were generated and automatically saved in the computer. With that data, it was possible to obtain plots that will be represented and analysed subsequently.

Based on the ignition method chosen, the average inlet mass flow rate was approximately 0.531 kg/s and there was only one rotating detonation wave in the combustion chamber. During the entire computing process, data was recorded to allow the analysis of the propagation information. Some of the properties at the inlet and exit plane, specifically the inlet mass flow rate (Figure 4.14), outlet pressure (Figure 4.15), outlet velocity (Figure 4.16), engine thrust (Figure 4.17), and mixture-based specific impulse (Figure 4.18) are plotted below. They show the development of the properties and engine performance over the simulation time. The beginning of the simulation (from 0 seconds until 0.0002116 seconds) is not represented because there was a problem with the recorded data from ANSYS. However, that does not represent a problem because the engine was initiating and it was not in stable operation yet.

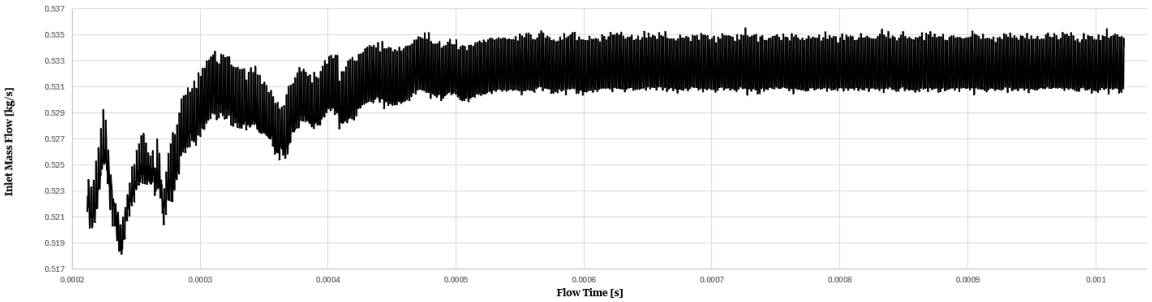

Figure 4.14: Development of Inlet Mass Flow Rate.

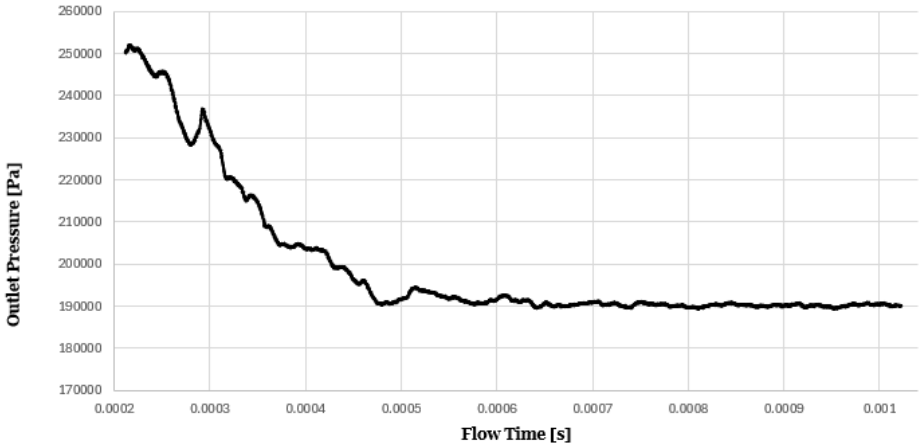

Figure 4.15: Development of Outlet Pressure.

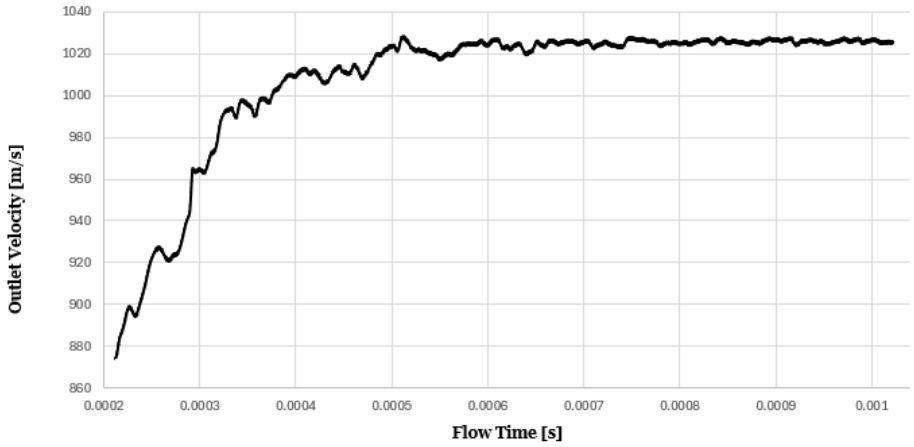

Figure 4.16: Development of Outlet Velocity.

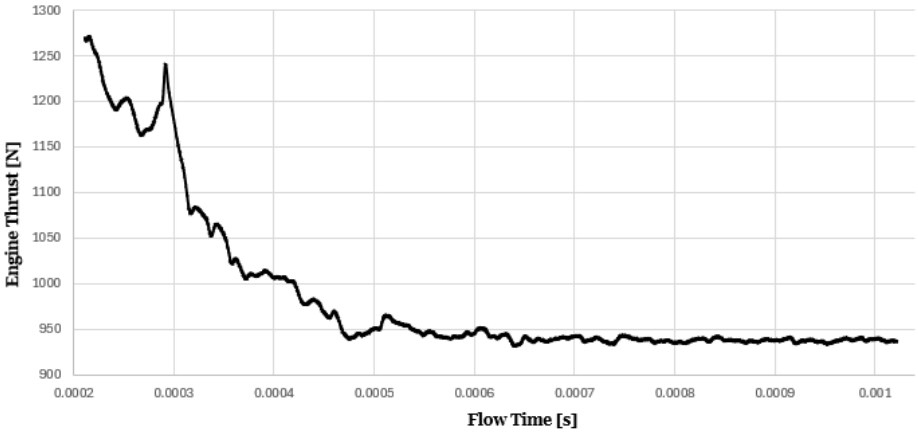

Figure 4.17: Propulsive Performance - Engine Thrust.

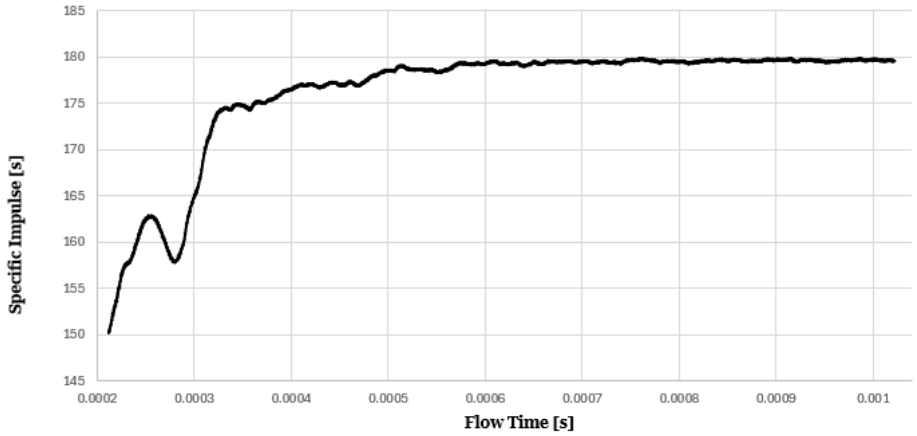

Figure 4.18: Propulsive Performance - Mixture-Based Specific Impulse.

The plots illustrate that the engine completely stabilizes its operation after 500 microseconds. Before that, there were variations of the properties but they tend to stabilize.

The thrust, F, and mixture-based specific impulse, I_{sp}, of the RDE were calculated as follows [54][69]:

$$F = \dot{m}\, V + p\, A \tag{4.1}$$

$$I_{sp} = \frac{F}{\dot{m} g} \tag{4.2}$$

where $\dot{m}$ is the outlet mass flow rate, the V is the outlet velocity, the p is the outlet pressure, the A is the area of the outlet and the g is the gravitational acceleration.

The engine thrust in stable operation was around 940 newtons and the specific impulse was around 179 seconds. The thrust and the specific impulse show some small fluctuations, which might be caused

by the interaction between the detonation wave and the injection process.

The obtained values were compared to results from other simulations and that comparison is shown in Table 4.1. Of the results presented in Table 4.1, it is worth highlighting that they are close to the results obtained in the present work which validates the results and confirms the accuracy of the simulation.

Table 4.1: Comparison between Simulation Values and Reference Values.

Studied Simulation	$F = 940N$	$I\_sp = 179s$
Reference 1 [54]	$F = 848.4N$	$I\_sp = 173s$
Reference 2 [54]	$F = 813.6N$	$I\_sp = 165.9s$
Reference 3 [70]	$F = 680N$	$I\_sp = 200.4s$

Figure 4.19 shows the contributions of the two parcels of the thrust equation for the thrust value. The contribution of the first parcel of the equation 4.1 is represented in Figure 4.19 in black (momentum contribution) and the contribution of the other parcel is shown in orange (pressure contribution).

Two interesting conclusions can be taken. First, the momentum contribution is higher than the pressure contribution. Second, the pressure contribution line suffers fewer variations, presenting itself as more stable than the momentum contribution line which means there are more variations in the parameters of the first parcel of Equation 4.1.

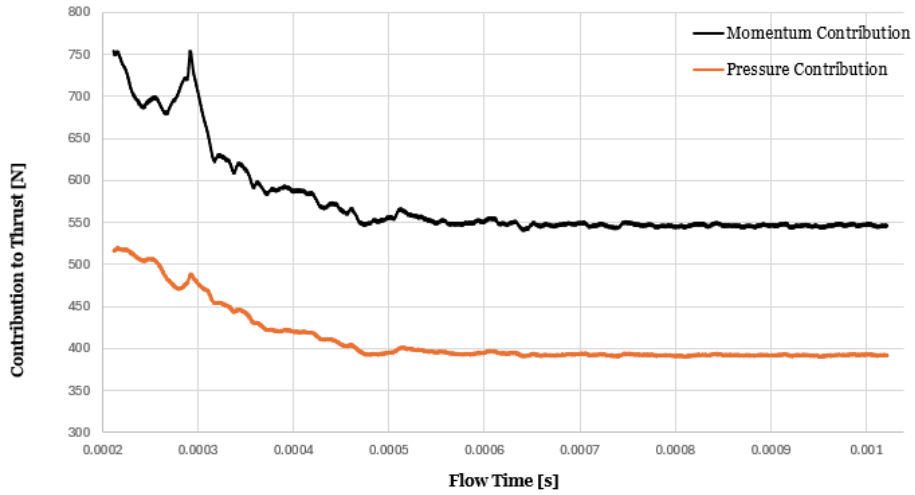

Figure 4.19: Momentum and Pressure Contributions to Thrust.

Three monitor points were set between the outer and inner walls of the combustion chamber for each case. The first point was located in the inlet, between two evenly spaced injectors, the second point was located 40 mm from the inlet and the third point was in the outlet. The pressure of these points was recorded during the whole computing process to obtain the propagation information of the rotating detonation wave. When the detonation wave passes these points, their pressure record curves will present a peak, as shown in Figure 4.20. There are five peaks which means that the detonation wave passed five times through the monitor points.

Furthermore by looking at Figure 4.20, we can see a significant pressure difference when the detonation wave passes. In Figure 4.22 we can easily identify where the detonation front is because the pressure difference is so significant. That is the reason why the detonation wave front is represented in red to green colors and the rest of the chamber is blue.

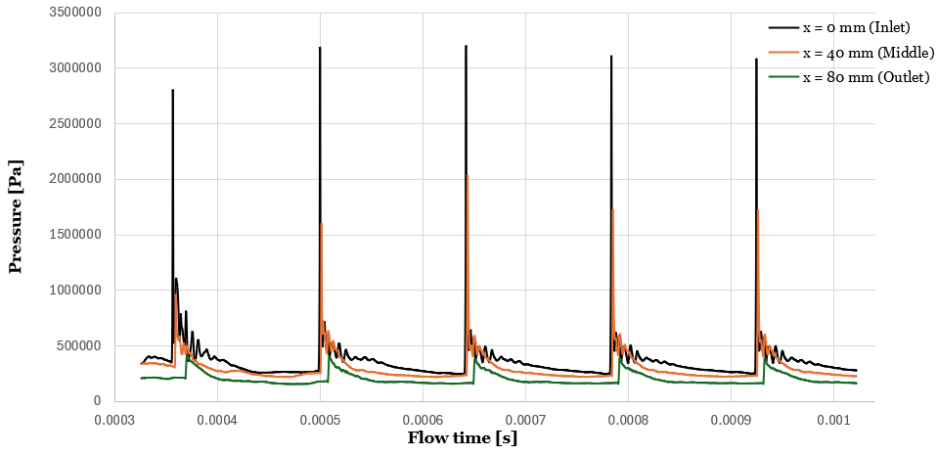

Figure 4.20: Pressure Record Curves of the Monitor Points.

From Figure 4.20 we can see that the detonation wave propagates continuously during the operation time. The time intervals for each revolution are shown in Table 4.2. Additionally, Figure 4.20 shows similarities with Figure 2.16 displayed in Subsection 2.5.3, giving another proof of the simulation results validity and accuracy.

Table 4.2: Time of each revolution .

Revolution 1	143.2 μs
Revolution 2	142.1 μs
Revolution 3	141.6 μs
Revolution 4	141.1 μs

The mean diameter of the combustion chamber is 87.5 mm, so the perimeter is 274.89 mm. Thus the detonation propagation velocities are calculated as 1919.62 m/s for the first revolution, 1934.48 m/s for the second revolution, 1941.31 m/s for the third revolution and 1948.19 m/s for the fourth revolution.

The simulation ran for approximately 47 days non-stop, the total simulation time was 1022 microseconds, with 10220 time steps and 511000 iterations.

4.5 Overview of the Detonation Wave Inside the Chamber

With the objective of enhancing the understanding of the detonation wave movement inside the annular combustion chamber, this section will display three sets of Figures (4.21 to 4.23) showing an overview of the temperature, pressure and H2 mass fraction parameters during the third revolution. Each set will be displayed in a single dedicated page.

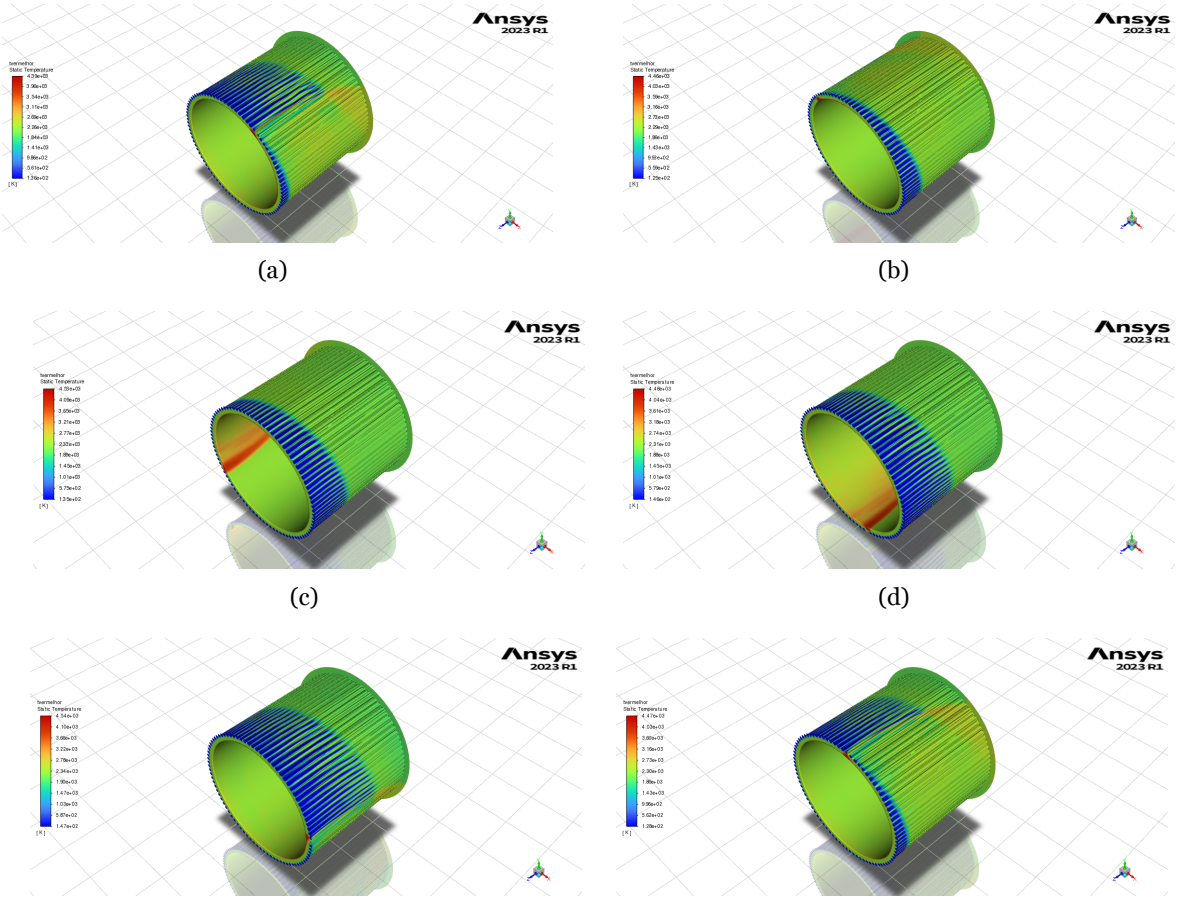

(a) (b)

(c) (d)

(e) (f)

Figure 4.21: Contours of Temperature: (a) 641 μs; (b) 669.4 μs ; (c) 697.8 μs; (d) 726.2 μs; (e) 754.6 μs; (f) 783 μs.

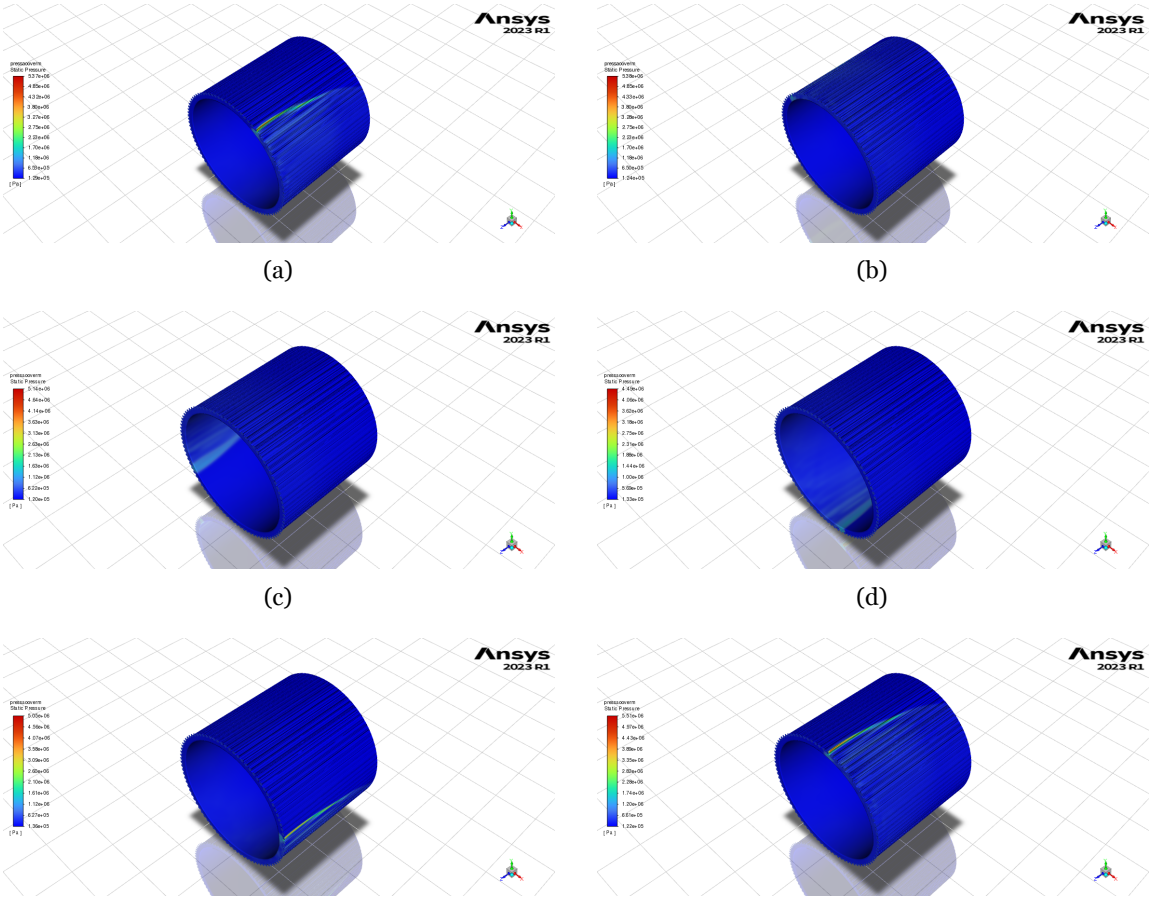

(a) (b)

(c) (d)

(e) (f)

Figure 4.22: Contours of Pressure: (a) 641 μs; (b) 669.4 μs ; (c) 697.8 μs; (d) 726.2 μs; (e) 754.6 μs; (f) 783 μs.

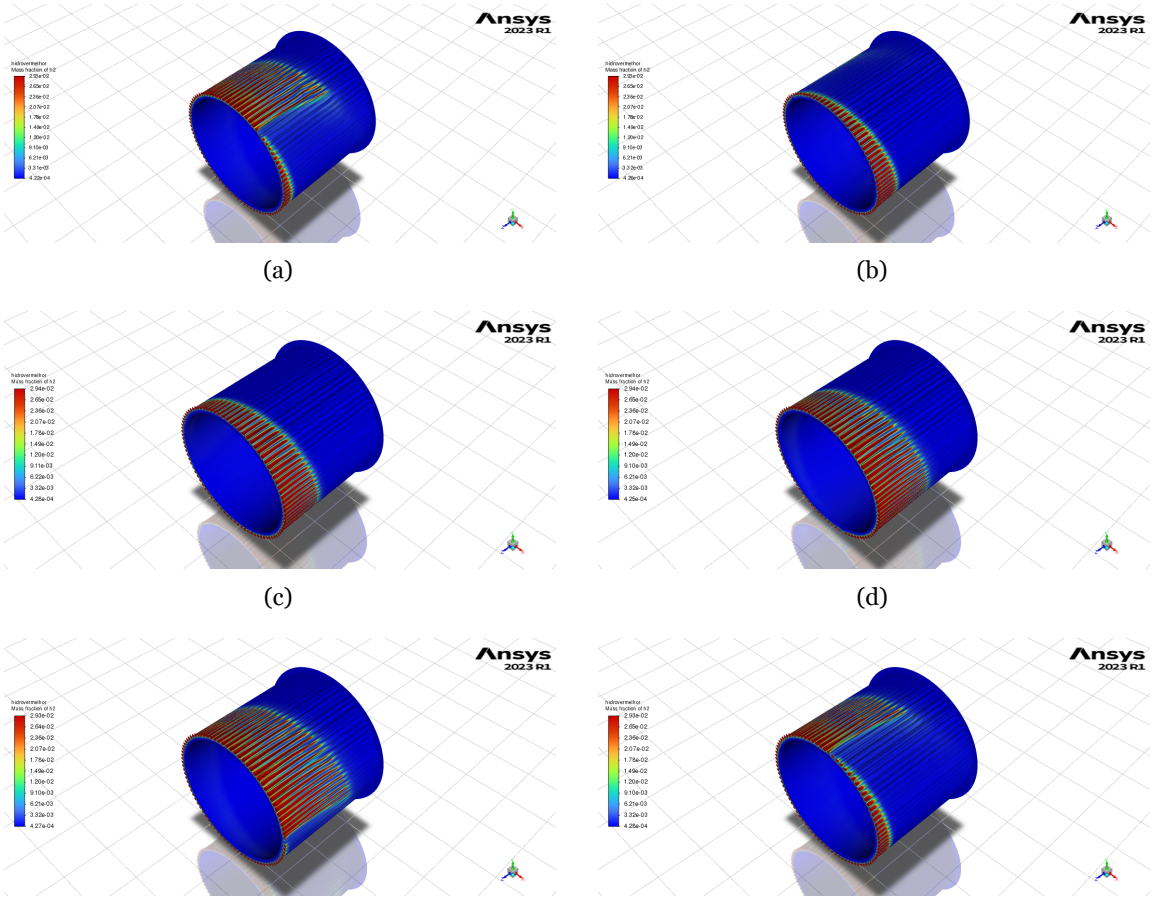

(a) (b)

(c) (d)

(e) (f)

Figure 4.23: Contours of H2 mass fraction: (a) 641 μs; (b) 669.4 μs ; (c) 697.8 μs; (d) 726.2 μs; (e) 754.6 μs; (f) 783 μs.

4.6 Results Summary

A stable operation of a rotating detonation engine using a mixture of hydrogen and air was obtained. An initial detonation wave appeared inside the chamber near the ignition zone where the patch was created. This wave appeared in both simulations (either using hydrogen and air or hydrogen and oxygen). Counter-rotating waves also appear in both simulations a few time steps later. When using a mixture of hydrogen and air, the waves' fronts were straighter and taller compared to the ones that appeared when a mixture of hydrogen and oxygen was used. Also, the maximum static pressure was almost two times greater when using oxygen instead of air.

It was found that reversed flow in the inlet occurred at each time step. This phenomenon has been reported in many other articles and is still being studied by many researchers and students. In this simulation, some high pressure combustion products that would produce thrust were lost, but the effect of reverse flow was small because only a relatively small percentage in each instant was, in fact, in backflow and the impact on the accuracy of the simulation and on the efficiency of the engine was low.

The simulation using a mixture of hydrogen and oxygen did not reach stable operation. Instead of detonation, a shock with no coupled chemistry occurred. When using a mixture of hydrogen and air, the engine reached stable operation and the detonation wave travelled inside the combustion chamber performing four revolutions. Only one detonation wave was travelling inside the chamber and the average inlet mass flow rate was approximately 0.531 kg/s. The average thrust during stable operation was 940 N and the mixture-based specific impulse was 179 s. These results were validated with results from other studies. Concerning the thrust value, it was found that the momentum contribution is higher than the pressure contribution, and the pressure contribution line suffers fewer variations, presenting itself as more stable than the momentum contribution line.

Three monitor points were set between the outer and inner walls of the combustion chamber for each case which recorded important simulation data. It was found that the average time per revolution was around 142 microseconds and the average detonation wave propagation velocity calculated was around 1935.90 m/s.

Chapter 5

Conclusion

5.1 Summary

The objectives outlined in this dissertation have been successfully achieved. A strong theoretical foundation was established, encompassing key topics such as combustion, detonation, and computational fluid dynamics (CFD). Moreover, a thorough review of the state-of-the-art in RDEs was conducted, covering historical developments, current characteristics, limitations, and recent advancements, making it a valuable reference for future consultation.

A methodology was followed and validated to obtain an operating simulation of a rotating detonation engine using ANSYS Fluent. The results were compared against other numerical simulations, confirming its accuracy and reliability. The full CFD process was implemented successfully, and some conclusions were reached.

The simulation using a mixture of hydrogen and oxygen did not evolve to continuous detonation and deflagration happened. When using a mixture of hydrogen and air, detonation occurred and the engine reached stable operation. During stable operation, the average thrust was 940 newtons, the average mixture-based specific impulse was 179 seconds, the time between revolutions was about 142 microseconds and the detonation velocities were around 1936 m/s.

As a final note, working on this subject was very enlightening regarding RDE's operation and the theory behind CFD simulations. Despite all the challenges and difficulties found throughout the work, I have developed my problem-solving skills and learned a lot about this next-generation propulsion technology.

5.2 Limitations

There were two major limitations in this work: time and computational resources. This work was supposed to be completed within a single semester, allowing for roughly four months of work. These limitations posed significant challenges, particularly in selecting appropriate simulation geometry, refining the mesh, and adjusting parameter settings to ensure convergence of the results.

Furthermore, each simulation required a substantial amount of time, often taking three to four weeks to produce accurate and analyzable data making this the most difficult challenge of all. However, the project yielded valuable insights and conclusions.

5.3 Future Work

There is still much to investigate about RDEs. Future developments regarding this area can be focused on the following items:

- Implementing more sophisticated and detailed chemical kinetics models, including reaction mechanisms with a broader range of intermediate species and reactions to better capture the detonation process under various operating conditions;
- Using other high-fidelity turbulence models (for example Large Eddy Simulation) because they can offer deeper insights into the turbulent mixing and flame stabilization mechanisms, which are critical for efficient and stable operation;
- Optimizing various design parameters, such as the injectors configurations, fuel-oxidizer ratios, and a more complex combustor geometry, to approximate as much as possible to the reality with the use of more computational power;
- Assessing the environmental impact of RDEs, including emissions and noise pollution. Future studies should quantify these impacts and develop strategies for minimizing them. Also, investigating alternative fuels, such as biofuels, could enhance their environmental sustainability and performance. This involves studying the combustion characteristics and detonation behaviour of these fuels within the engine;
- Building real-scale prototypes and conducting experiments to gather empirical data to help calibrate and validate the simulation results, ensuring their accuracy and reliability.

Bibliography

[1] AFRL. Rotating detonation engines (RDE). [Online]. Available: https://afresearchlab.com/technology/rotating-detonation-engines-rde/ 1

[2] M. Zhao, L. Zhang, W. Huo, H. Yang, and Y. Yuan, "Performance analysis of a rotating detonation model for future thermal power system using hydrogen as fuel," *Energy Reports*, vol. 8, pp. 66–74, 2022, 2021 6th International Conference on Clean Energy and Power Generation Technology. [Online]. Available: https://www.sciencedirect.com/science/article/pii/S235248472101180X 1, 17, 18, 19

[3] L. Su, F. Wen, S. Wang, and Z. Wang, "Analysis of energy saving and thrust characteristics of rotating detonation turbine engine," *Aerospace Science and Technology*, vol. 124, p. 107555, 2022. [Online]. Available: https://www.sciencedirect.com/science/article/pii/S1270963822002292 1

[4] K. Mcalpine, "Rotating detonation engine: The old is new again," *Michigan Engineering News*, March 2017. [Online]. Available: https://news.engin.umich.edu/2017/03/rotating-detonation-engine-the-old-is-new-again/ 5, 6

[5] M. Gamba. Rotating detonation engines. Michigan Engineering, Gas Dynamics Imaging Laboratory. [Online]. Available: https://gdilab.engin.umich.edu/rotating-detonation-engines/ 5

[6] J. Sweeney. (December 2009) Pulse detonation engines. [Online]. Available: https://www.colorado.edu/faculty/kantha/sites/default/files/attached-files/sweeney.pdf 5

[7] P. Wolański, "Detonation engines," *Journal of KONES Powertrain and Transport*, vol. 18, pp. 515–521, 01 2011. 5, 6, 19, 20, 21, 22, 23, 24

[8] R. Osorio. (January 2023) NASA validates revolutionary propulsion design for deep space missions. [Online]. Available: https://www.nasa.gov/centers-and-facilities/marshall/nasa-validates-revolutionary-propulsion-design-for-deep-space-missions/ 6

[9] National Museum of The United States Air Force. AFRL pulsed detonation engine. [Online]. Available: https://www.nationalmuseum.af.mil/Visit/Museum-Exhibits/Fact-Sheets/Display/Article/628269/afrl-pulsed-detonation-engine/ 6

[10] P. Ligrani, E. McNabb, H. Collopy, M. Anderson, and M. S. Marko, "Recent investigations of shock wave effects and interactions," *Advances in Aerodynamics*, vol. 2, 12 2020. [Online]. Available: https://www.researchgate.net/publication/339105584_Recent_investigations_of_shock_wave_effects_and_interactions 7

[11] J. D. Anderson Jr., *Fundamentals of Aerodynamics (6th edition)*. McGraw-Hill Education, March 2016. 7, 8, 9, 10, 11, 12

[12] NASA. (February 2019) Schlieren supersonic shock waves. [Online]. Available: https://www.nasa.gov/image-detail/f4_p4_plane_drop_v/ 7

[13] V. Nikonov, "A semi-lagrangian godunov-type method without numerical viscosity for shocks," *Fluids*, vol. 7, no. 1, 2022. [Online]. Available: https://www.mdpi.com/2311-5521/7/1/16 7

[14] R. W. Fox, A. T. McDonald, and P. J. Pritchard, *Introduction to Fluid Mechanics (6th edition)*. John Wiley & Sons, Inc., 2004. 7, 8, 9, 11

[15] A. A. Vasil'ev, "Rotating detonation: History, results, problems," *Transactions on Aerospace Research*, vol. 2020, no. 4, pp. 48–60, 2020. [Online]. Available: https://doi.org/10.2478/tar-2020-0020 13

[16] P. W. Copper, *Explosives Engineering*. Wiley-VCH, 1996. 13

[17] R. Driscoll, "Experimental investigation of shock transfer and shock initiated detonation in a dual pulse detonation engine crossover system," Ph.D. dissertation, 09 2013. [Online]. Available: https://www.researchgate.net/publication/271199012_EXPERIMENTAL_INVESTIGATION_OF_SHOCK_TRANSFER_AND_SHOCK_INITIATED_DETONATION_IN_A_DUAL_PULSE_DETONATION_ENGINE_CROSSOVER_SYSTEM 14

[18] K. Kuo, *Principles of Combustion*. Wiley, 1986. 14

[19] V. N. Kondratiev. (February 2024) combustion. [Online]. Available: https://www.britannica.com/science/combustion 14, 15, 16

[20] N. Hall. (May 2021) Combustion. Glenn Research Center. [Online]. Available: https://www.grc.nasa.gov/www/k-12/airplane/combst1.html 15

[21] A. P. John. (January 2023) Types of combustion: Meaning and examples. [Online]. Available: https://www.embibe.com/exams/types-of-combustion/ 16

[22] B. O'Connor. (March 2023) Explosions, deflagrations, and detonations. National Fire Protection Association. [Online]. Available: https://www.nfpa.org/news-blogs-and-articles/blogs/2023/03/27/explosions-vs-deflagrations-vs-detonations 16, 17

[23] P. Wolański, "Detonative propulsion," *Proceedings of the Combustion Institute*, vol. 34, no. 1, pp. 125–158, 2013. [Online]. Available: https://www.sciencedirect.com/science/article/pii/S1540748912004014 17, 18, 19, 21, 22, 23, 24

[24] Aerodynamics Research Center. (2014) Pulsed detonation engines. University of Texas at Arlington, Mechanical and Aerospace Engineering. [Online]. Available: https://arc.uta.edu/research/pde.htm 19

[25] G. Matloff and H. Gerrish, "Chapter 3 - the scale of the problem: Interstellar distances, time, and energy considerations," in *Interstellar Travel*, L. Johnson and K. Roy, Eds. Elsevier, 2023, pp. 51–82. [Online]. Available: https://www.sciencedirect.com/science/article/pii/B978032391360700001X 20

[26] J. A. Nicholls, H. R. Wilkinson, and R. B. Morrison, "Intermittent detonation as a thrust-producing mechanism," *Journal of Jet Propulsion, 27 (5), 534–541*, 1957. 20

[27] T. Bussing and G. Pappas, *An introduction to pulse detonation engines*. [Online]. Available: https://arc.aiaa.org/doi/abs/10.2514/6.1994-263 21

[28] R. Dunlap, R.L. Brehm, J.A. Nicholls, "A preliminary study of the application of steady-state detonative combustion to a reaction engine," *Journal of Jet Propulsion, 28 (7), 451–456*, 1958. 21

[29] J. Koch, M. Kurosaka, C. Knowlen, and J. N. Kutz, "Mode-locked rotating detonation waves: Experiments and a model equation," *Physical Review E*, vol. 101, no. 1, jan 2020. [Online]. Available: http://dx.doi.org/10.1103/PhysRevE.101.013106 22

[30] P. Wolański, in *G. D. Roy, S. M. Frolov (Eds.), Deflagrative and Detonative Combustion*. Torus Press, Moscow, 2010, pp. 395–406. 22

[31] F. A. Bykovskii, and S. A. Zhdan, “Continuous spin detonation of a hydrogen-air mixture in the air ejection mode,” *Detonation Wave Propulsion Workshop, Bourges, France*, July 2011. 23

[32] H. H. Hu, “Chapter 10 - computational fluid dynamics,” in *Fluid Mechanics (Fifth Edition)*, fifth edition ed., P. K. Kundu, I. M. Cohen, and D. R. Dowling, Eds. Boston: Academic Press, 2012, pp. 421–472. [Online]. Available: https://www.sciencedirect.com/science/article/pii/B9780123821003100101 24, 27

[33] J. Anderson, *Computational Fluid Dynamics: The Basics with Applications*, ser. McGraw-Hill International Editions: Mechanical Engineering. McGraw-Hill, 1995. [Online]. Available: https://books.google.pt/books?id=phG_QgAACAAJ 24, 25, 26

[34] H. K. Versteeg and W. Malalasekera, *An introduction to computational fluid dynamics - the finite volume method*. Addison-Wesley-Longman, 1995. 24, 25, 27

[35] J. Martin and S. Mccutcheon, *Hydrodynamics and Transport for Water Quality Modeling*, 11 1998. 27, 28

[36] MIT. Basics of turbulent flow. [Online]. Available: https://web.mit.edu/1.061/www/dream/SEVEN/SEVENTHEORY.PDF 27

[37] IdealSimulations. (2020) Turbulence models in cfd. [Online]. Available: https://www.idealsimulations.com/resources/turbulence-models-in-cfd/ 27

[38] Cadence CFD. The Reynolds-Averaged Navier-Stokes (RANS) Equations and Models. [Online]. Available: https://resources.system-analysis.cadence.com/blog/msa2021-the-reynolds-averaged-navier-stokes-rans-equations-and-models 28

[39] L. Davidson, “An introduction to turbulence models,” vol. 97/2, August 2022. [Online]. Available: https://www.tfd.chalmers.se/~lada/postscript_files/kompendium_turb.pdf 28

[40] Altair. (2023) Reynolds-Averaged Navier-Stokes (RANS) Simulations. [Online]. Available: https://help.altair.com/hwcfdsolvers/acusolve/topics/acusolve/training_manual/rans_simulations_r.htm 28, 29

[41] Altair. (2023) Large Eddy Simulation (LES). [Online]. Available: https://help.altair.com/hwcfdsolvers/acusolve/topics/acusolve/training_manual/large_eddy_simulation_r.htm 29

[42] SimScale. (December 2023) What is Large Eddy Simulation (LES) in CFD? [Online]. Available: https://www.simscale.com/docs/simwiki/cfd-computational-fluid-dynamics/large-eddy-simulation-les/ 29

[43] Altair. (2023) Direct Numerical Simulation. [Online]. Available: https://help.altair.com/hwcfdsolvers/acusolve/topics/acusolve/training_manual/direct_numerical_simulation_r.htm 29

[44] Altair. (2023) Zero-Equation Eddy Viscosity Models. [Online]. Available: https://help.altair.com/hwcfdsolvers/acusolve/topics/chapter_heads/zero_eqn_eddy_visc_models_r.htm#reference_sby_bmn_xw 30

[45] Altair. (2023) One Equation Eddy Viscosity Models. [Online]. Available: https://help.altair.com/hwcfdsolvers/acusolve/topics/acusolve/training_manual/one_eq_eddy_visc_models_r.htm#reference_zw2_4wy_dw 30

[46] Altair. (2023) Standard $k-\varepsilon$ model. [Online]. Available: https://help.altair.com/hwcfdsolvers/acusolve/topics/acusolve/training_manual/standard_k_e_model_r.htm 30

[47] ANSYS. (January 2009) RNG k- ε model. [Online]. Available: https://www.afs.enea.it/project/neptunius/docs/fluent/html/th/node59.htm 30

[48] ANSYS. (January 2009) Realizable k- ε model. [Online]. Available: https://www.afs.enea.it/project/neptunius/docs/fluent/html/th/node60.htm 31

[49] ANSYS. (January 2009) Standard k- ω model. [Online]. Available: https://www.afs.enea.it/project/neptunius/docs/fluent/html/th/node66.htm 31

[50] ANSYS. (January 2009) Shear-stress transport (SST) k- ω model. [Online]. Available: https://www.afs.enea.it/project/neptunius/docs/fluent/html/th/node67.htm 31

[51] J. W. Slater. (February 2021) CFD analysis process. National Program for Applications-Oriented Research in CFD - Alliance CFD Verification and Validation Website. [Online]. Available: https://www.grc.nasa.gov/www/wind/valid/tutorial/process.html 31

[52] P. Pal, G. Kumar, S. Drennan, B. Rankin, and S. Som, "Multidimensional numerical modeling of combustion dynamics in a non-premixed rotating detonation engine with adaptive mesh refinement," *Journal of Energy Resources Technology*, vol. 143, p. 112308, 03 2021. [Online]. Available: https://www.researchgate.net/publication/349898682_Multidimensional_Numerical_Modeling_of_Combustion_Dynamics_in_a_Non-Premixed_Rotating_Detonation_Engine_With_Adaptive_Mesh_Refinement 36, 44

[53] J. Koch, M. Kurosaka, C. Knowlen, and J. N. Kutz, "Multiscale physics of rotating detonation waves: Autosolitons and modulational instabilities," *Physical Review E*, vol. 104, no. 2, aug 2021. [Online]. Available: http://dx.doi.org/10.1103/PhysRevE.104.024210 36

[54] J. Sun, J. Zhou, S. Liu, and Z. Lin, "Numerical investigation of a rotating detonation engine under premixed/non-premixed conditions," *Acta Astronautica*, vol. 152, pp. 630–638, 2018. [Online]. Available: https://www.sciencedirect.com/science/article/pii/S0094576518314450 36, 44, 46, 59, 60

[55] M. Folusiak, A. Kobiera, and P. Wolański, "Rotating detonation engine simulations in-house code – reflops," *Institute of Aviation*, 2010. 36

[56] A. St. George, R. Driscoll, V. Anand, S. Randall, D. Munday, and E. Gutmark, "Development of a rotating detonation engine facility at the university of cincinnati," 01 2015. [Online]. Available: https://www.researchgate.net/publication/271199030_Development_of_a_Rotating_Detonation_Engine_Facility_at_the_University_of_Cincinnati 36

[57] Z. Sun, Y. Huang, Z. Luan, S. Gao, and Y. You, "Three-dimensional simulation of a rotating detonation engine in ammonia/hydrogen mixtures and oxygen-enriched air," *International Journal of Hydrogen Energy*, vol. 48, no. 12, pp. 4891–4905, 2023. [Online]. Available: https://www.sciencedirect.com/science/article/pii/S0360319922052156 36, 46

[58] ANSYS. (April 2016) Introduction to ansys fluent - lecture 9: Best practice guidelines. [Online]. Available: https://www.kth.se/social/files/57149285f27654646b25d53b/05-Quality-ANSYS.pdf 37, 38

[59] G. A. Muñoz. (February 2015) Mesh quality and advanced topics ansys workbench 16.0. [Online]. Available: https://www.academia.edu/16970000/MESH{_}QUALITY{_}AND{_}ADVENCED{_}TOPICS{_}ANSYS{_}WORKBENCH{_}16.0 37, 42

[60] T. Avraham. (February 2019) Know thy mesh – mesh quality – part I. [Online]. Available: https://cfdisraelblog.com/2019/02/01/mesh/ 38, 39

[61] ANSYS. (2020) Fluent user's guide. [Online]. Available: https://ansyshelp.ansys.com/account/secured?returnurl=/Views/Secured/corp/v202/en/flu_ug/flu_ug.html 43

[62] ANSYS, Inc. (December 2010) Lecture 5 solver settings - introduction to ansys fluent. [Online]. Available: https://imechanica.org/files/fluent_13.0_lecture05-solver-settings.pdf 45, 46, 47

[63] A. Singh and S. Mukhopadhyay, "Comparison of pressure-based and density-based solvers for scramjet modeling," *AIP Conference Proceedings*, vol. 2584, no. 1, p. 030007, 05 2023. [Online]. Available: https://doi.org/10.1063/5.0128250 46

[64] J. Li, J. Yu, J. Li, Y. Lei, S. Yao, and W. Zhang, "Investigation of hydrogen-enriched kerosene-fueled rotating detonation engine with multi-column film cooling," *Physics of Fluids*, vol. 36, no. 1, p. 016138, 01 2024. [Online]. Available: https://doi.org/10.1063/5.0181011 48

[65] N. Smirnov, V. Nikitin, L. Stamov, E. Mikhalchenko, and V. Tyurenkova, "Three-dimensional modeling of rotating detonation in a ramjet engine," *Acta Astronautica*, vol. 163, pp. 168–176, 2019, space Flight Safety-2018. [Online]. Available: https://www.sciencedirect.com/science/article/pii/S0094576518321817 54

[66] N. N. Smirnov, V. F. Nikitin, L. I. Stamov, E. V. Mikhalchenko, and V. V. Tyurenkova, "Rotating detonation in a ramjet engine three-dimensional modeling," *Aerospace Science and Technology*, vol. 81, pp. 213–224, 2018. [Online]. Available: https://www.sciencedirect.com/science/article/pii/S1270963818316924 54

[67] K. Goto, R. Yokoo, A. Kawasaki, K. Matsuoka, J. Kasahara, A. Matsuo, I. Funaki, and H. Kawashima, "Investigation into the effective injector area of a rotating detonation engine with impact of backflow," *Shock Waves 31, 753–762 (2021)*. [Online]. Available: https://link.springer.com/article/10.1007/s00193-021-00998-9 54

[68] D. E. Paxson and K. Miki, "Computational assessment of inlet backflow effects on rotating detonation engine performance and operability," *NASA Glenn Research Center, Cleveland, Ohio, 44135, USA*, 2022. [Online]. Available: https://ntrs.nasa.gov/citations/20210024739 54

[69] N. Hall, "Rocket thrust equation," *NASA Glenn Research Center*, May 2021. [Online]. Available: https://www.grc.nasa.gov/www/k-12/airplane/rockth.html 59

[70] I. J. Shaw, J. A. Kildare, M. J. Evans, A. Chinnici, C. A. Sparks, S. N. Rubaiyat, R. C. Chin, and P. R. Medwell, "A theoretical review of rotating detonation engines," in *Direct Numerical Simulations*, S. Rao, Ed. Rijeka: IntechOpen, 2019, ch. 7. [Online]. Available: https://doi.org/10.5772/intechopen.90470 60

Appendix A

User-Defined Function

```
DEFINE_PROFILE(initial_pressure,th,i)
{
face_t f;
Domain *d = Get_Domain(1);
Thread *t = Lookup_Thread(d,5);
real po;
real pcr;
real To;
real gamma;
real R;
real p_cur;
po = 1013250; // stagnation pressure
gamma = 1.4;
pcr = po * pow(2/(gamma + 1), gamma/(gamma-1)); // critical pressure
To = 300; // stagnation temperature
R = 368.9; // J/kg k

#if !RP_HOST

begin_f_loop(f,th)
{

p_cur = F_P(f,th); //pressure on one face

if(p_cur >= po)
F_PROFILE(f,th,i) = po;

else if(p_cur <= po && p_cur > pcr)

F_PROFILE(f,th,i) = p_cur;

else if(p_cur <= pcr)
F_PROFILE(f,th,i) = pcr;

}
end_f_loop(f,th)
#endif

}
```